Unshielded precipitation gauge collection efficiency with wind speed and hydrometeor fall velocity. Part I: modelling results

Jeffery Hoover[1], Pierre E. Sullivan[2], Paul I. Joe[1], Michael E. Earle[1]

[1]Environment and Climate Change Canada, Toronto, ON, M3H 5T4, Canada
5   [2]Department of Mechanical and Industrial Engineering, University of Toronto, Toronto, ON, M5S 3G8, Canada

Correspondence to: Jeffery Hoover (jeffery.hoover@canada.ca)

Abstract. A new method for assessing collection efficiency using wind speed and hydrometeor fall velocity is presented for the unshielded Geonor T-200B3 precipitation gauge based on computational fluid dynamics results. Time-averaged Navier-Stokes simulations with a k-ε turbulence model were used to determine the airflow around the gauge for 0 to 10 m s^{-1} wind

10   speeds. Hydrometeor trajectories and collection efficiencies were determined using Lagrangian analysis for spherical hydrometeor fall velocities between 0.25 to 10 m s^{-1} for rain (0.01 – 3.9 mm diameter), wet snow (0.2 – 21 mm diameter), dry snow (0.2 - 7.1 mm diameter), and ice pellets (1.5 – 4.3 mm diameter). The model results demonstrate that gauge collection efficiency strongly depends on both wind speed and hydrometeor fall velocity. Collection efficiency differences for identical hydrometeor fall velocities are within 0.05 for wind speeds less than 4 m s^{-1}, despite differences in hydrometeor type, diameter,

15   density, and mass. An empirical expression for collection efficiency with dependence on wind speed and fall velocity is presented based on the numerical results, giving a RMSE of 0.03 for dry snow, wet snow, and rain, for wind speeds between 0 and 10 m s^{-1}. The use of fall velocity captures differences in collection efficiency due to different hydrometeor types and sizes, and can be broadly applied even where the precipitation type may be unknown or uncertain. Results are compared to previous models and good model agreement with experimental results is demonstrated in Part II.

1 Introduction

Automated catchment-type precipitation gauge measurements are commonly used for weather, climate, hydrology, and transportation applications. A variety of gauge types and shield configurations are used worldwide (Nitu, 2010), with

25 unshielded gauges installed by many users, particularly in remote locations and harsh environments, as they are lower cost, require less maintenance, and are easier to install than shielded configurations. The systematic bias of measurements from unshielded gauges due to wind-induced undercatch and other factors, however, is more significant than for shielded configurations. This presents a major challenge for unshielded gauge users, particularly for the measurement of solid precipitation.

30 The collection efficiency (CE) for solid precipitation – the ratio of the gauge measurement to the "true" or reference value – decreases with increasing wind speed, and more rapidly for unshielded gauges compared to shielded gauges (Rasmussen et al., 2012;Nitu et al., 2018). Precipitation gauge intercomparisons have demonstrated that an unshielded weighing gauge can capture less than 50 % of the actual amount of solid precipitation falling in air for wind speeds exceeding 5 m s^{-1} (Kochendorfer et al., 2017). Various adjustments for precipitation amount and type (liquid, solid, and mixed) have been proposed using wind

35 speed and most recently temperature (Kochendorfer et al., 2018;Goodison et al., 1998;Wolff et al., 2015;Smith, 2007). These adjustments have reduced the systematic bias of gauge undercatch with wind speed, but only marginally improved the uncertainty (Kochendorfer et al., 2018). This limitation is not well understood, and may be due to variations in solid precipitation characteristics, wind speed, turbulence, or other factors.

For rainfall, the relationship between hydrometeor mass, equivalent spherical diameter, and terminal velocity is well

40 understood (Beard and Pruppacher, 1969;Laws, 1941;Gunn and Kinzer, 1949). The size distribution of raindrops is generally given by a negative exponential (Marshall and Palmer, 1948) or gamma drop size distribution based on the rainfall type (orographic, thunderstorm, stratiform, showers) and rainfall intensity (Ulbrich, 1983). The rainfall intensity is related to the hydrometeor size distribution, with increasing intensities corresponding to larger proportions of drops with larger sizes (Marshall and Palmer, 1948). The rainfall type also determines the shape of the distribution; for example, orographic rain has

45 more hydrometeors below 0.5 mm relative to thunderstorm rain (Ramana et al., 1959;Blanchard, 1953).

For solid precipitation, a wide variety of shapes, densities, and fall velocities are observed for different crystal types (Rasmussen et al., 1998;Khvorostyanov and Curry, 2005). For dry (unrimed) and wet (rimed) spherical snowflakes, the fall velocity increases with the hydrometeor diameter based on a power law (Rasmussen et al., 1998). Wet snow has a fall velocity twice that of dry snow for hydrometeors of the same size. The density decreases with hydrometeor diameter based on a power

50 law (Rasmussen et al., 1998). Studies have shown that the fall velocity depends on the equivalent water drop diameter for specific crystal types, including dendrites, rimed dendrites, columns and plates, and mixtures of dendrites and plates (Langleben, 1954;Imai et al., 1955). The sizes of aggregate snowflakes vary with precipitation intensity, with lower intensities corresponding with a sharper decay and higher intercept of a negative exponential distribution (Gunn and Marshall, 1957).

For rainfall, Nešpor and Sevruk (1999) demonstrated differences in collection efficiency with rainfall type and intensity for
55   the British Meteorological Office Mk2 gauge, the Hellman gauge, and the ASTA automated tipping bucket gauge used in
Switzerland. They employed a three-dimensional finite volume model with Reynolds-averaged Navier-Stokes (RANS)
numerical simulations and a k-ε turbulence model (where k is the turbulent kinetic energy and ε is its dissipation rate) to
estimate the horizontal and vertical air velocity components and turbulent kinetic energy. Lagrangian analysis was performed
to derive hydrometeor trajectories. Hydrometeor trajectories were computed based on the relative hydrometeor to air velocity,
60   with the drag coefficient given as a function of the Reynolds number given by Beard (1976). The model results showed the
dependence of the wind-induced error (inverse of collection efficiency for a given drop size) on the drop diameter and wind
speed, with larger errors for smaller drop diameters and higher wind speeds. A hydrometeor size limit below which no
hydrometeors were captured by the gauge was also shown to vary with wind speed. The conversion factor (ratio of true to
measured precipitation intensity) was derived from the integral of the wind-induced error over all drop sizes in a given
65   distribution representing orographic rain, thunderstorm rain, stratiform rain and showers. These results demonstrated the
influence of the rate of rainfall, wind speed, and rainfall type, with increased errors for low rainfall rates and higher wind
speeds. Errors for orographic rain, with increased numbers of smaller drop sizes with lower terminal velocities, were larger
than for thunderstorm rain, with larger drop sizes and higher terminal velocities.

For solid precipitation, Thériault et al. (2012) performed a RANS k-ε computation fluid dynamics (CFD) analysis of the airflow
70   around a single-Alter shielded Geonor gauge for wind speeds from 0 to 10 m s^{-1}. Hydrometeor trajectories were computed
using the Lagrangian method for different ice crystal types using a constant drag coefficient over each hydrometeor path.
Collection efficiencies were derived for discrete sizes from 0.5 to 10 mm and shown to vary based on wind speed, hydrometeor
type, and size. Differences in dry snow and wet snow model results for collection efficiencies were attributed to the different
terminal velocities of dry and wet snow hydrometeors, which influenced their trajectories and their interaction with the airflow
75   around the gauge. Collection efficiencies were also shown to decrease with increasing magnitude of the size distribution slope
parameter, corresponding with fewer hydrometeors with larger size and higher terminal velocity. Based on this theoretical
work, Thériault et al. (2012) developed a collection efficiency transfer function based on wind speed for each of the crystal
types studied. Dry snow and wet snow model results were shown to capture the upper and lower bounds of solid precipitation
collection efficiencies observed experimentally.

80   Hydrometeor tracking models for solid precipitation were developed further by Colli et al. (2015), who defined the
hydrometeor drag based on the local particle-to-air Reynolds number using the drag values for crystals and spheres from
Khvorostyanov and Curry (2005). Collection efficiency values using this approach increased significantly relative to the
constant drag coefficient approach, with smaller differences between collection efficiency results for crystals and spheres for
the unshielded Geonor gauge. Colli et al. (2015) extended this work to demonstrate the influence of the size distribution slope
85   parameter, and developed a collection efficiency transfer function based on the wind speed for 0.25 mm^{-1}, 0.50 mm^{-1} and 1
mm^{-1} slope parameters.

Differences in collection efficiency results for different drag models were assessed in recent studies by Baghapour and Sullivan (2017). Their results demonstrated the influence of the drag model from low speed Stokes flow conditions to high speed flows with inertial effects. Notably, collection efficiency differences of up to 40 % between Stokes, constant drag coefficient, and
90   empirical drag models were observed for high winds and large snowflake sizes.

Collection efficiency results are also sensitive to how the orifice, gauge geometry, and shielding influence the airflow and turbulence generation around the gauge (Nešpor, 1996;Nešpor and Sevruk, 1999;Colli et al., 2016b;Colli et al., 2016a;Colli et al., 2018;Baghapour and Sullivan, 2017;Baghapour et al., 2017;Thériault et al., 2015;Colli, 2014). Adding further complexity, results also differ based on the specific numerical model employed. Constantinescu et al. (2007) showed that computationally
95   intensive large eddy simulation (LES) models are better able to estimate the turbulent kinetic energy compared with time-averaged RANS models around two MetOne rain gauges. Recent studies by Colli et al. (2016a) around the Geonor gauge showed that computationally intensive time-dependent Large Eddy Simulation (LES) models can better resolve the turbulence above the orifice rim, as well as the intensity and spatial extent of turbulence compared with RANS $k\text{-}\omega$ shear stress tensor (SST) models (where k is the turbulent kinetic energy and ω turbulent specific dissipation rate). Temporal variations in the
100   airflow resulted in variations in hydrometeor trajectories and collection efficiencies for dry snow and wet snow hydrometeors using a Lagrangian particle tracking model with a constant-drag coefficient over the hydrometeor trajectories. Collection efficiencies for dry snow and wet snow varied with hydrometeor size and wind speed.

Using a refined gauge geometry and RANS $k\text{-}\varepsilon$, RANS $k\text{-}\omega$ SST, and LES models, Baghapour et al. (2017) showed the velocity profile and eddy dynamics for the Geonor gauge with unshielded, single-Alter, and double-Alter shield configurations. While
105   shielding decreased the flow momentum above the gauge orifice, turbulence generation was also increased. This momentum reduction also corresponded with an increase in the effective area of downward velocity across the orifice area. Tilting the shield slats in a fixed configuration reduced the benefits, demonstrating the sensitivity of model results to the shield slat angle, which can vary considerably in windy conditions. Using a variable drag model based on the relative particle to air velocity, LES and RANS $k\text{-}\omega$ SST model differences were shown to increase with the degree of shielding and for smaller hydrometeor
110   sizes (Baghapour and Sullivan, 2017). Collection efficiencies using time-averaged RANS simulations and an empirical hydrometeor drag model, despite underestimating the magnitude of the turbulent intensity above the gauge orifice, provided good overall agreement with event-based experimental results.

While existing models have demonstrated how collection efficiencies vary with wind speed, hydrometeor type, and size, their application to the reduction of uncertainty in experimental adjustments is a challenge. For example, different models are
115   required for different hydrometeor types and sizes, with very different fall velocities and collection efficiencies. Further, in many cases, the actual hydrometeor type is unknown or uncertain. Other adjustments based on wind speed and air temperature do not directly capture the hydrometeor characteristics.

The present study uses a refined gauge geometry, structured mesh, k-ε time-averaged Navier-Stokes numerical model, empirical drag model based on the relative particle-to-air velocity, and high density hydrometeor injection from a horizontal

120   injection plane to characterize the influence of wind speed and hydrometeor fall velocity on collection efficiency. Collection efficiencies are shown to be similar across precipitation types with identical fall velocities, enabling the development of a computationally cost-effective, universally applicable, and quantitative method for adjusting unshielded precipitation gauge measurements. This adjustment can greatly reduce the uncertainty in collection efficiency estimates for various hydrometeor types and sizes. The unshielded precipitation gauge is selected for the analysis in order to: (1) be free from model assumptions

125   regarding the shield slat behaviour, which can influence model results; (2) assess challenging model conditions, with a wider range of collection efficiencies relative to shielded gauges; and (3) limit the magnitude of turbulence generation due to shielding, which can contribute to increased variability in experimental results.

    This paper is organized into five sections. Section 2 describes the computational fluid dynamics (CFD) model, the Lagrangian particle tracking and hydrometeor drag formulation, the hydrometeor characteristics, the fall velocity model, and the

130   computational set up. Sections 3 and 4 describe the results and discussion, respectively. A summary is provided in Sect. 5. A companion paper will compare model results with observations.

2 Method

2.1 Computational fluid dynamics model

    A high-resolution 3-dimensional computer aided design model of the Geonor T-200B3 600 mm capacity gauge (hereafter

135   Geonor gauge) with 2 m gauge orifice height was developed for the analysis using SolidWorks engineering software (Figs. 1a and b). The Geonor gauge was modelled with a 200 cm^2 orifice, 3.15 mm orifice thickness, and full 360 mm length inlet extending down into the gauge housing. SolidWorks Flow Simulation software (SolidWorks, 2019) was used to simulate the time-averaged 3-dimensional flow around the unshielded precipitation gauge. Favre-averaged Navier-Stokes equations were used to relate the fluid density, velocity components, viscous shear stress, Reynolds (turbulence) stress tensor, and mass

140   distributed external force per unit mass, with contributions from porous media resistance, gravitational acceleration, and the coordinate systems rotation. The fluid was modelled as isothermal and incompressible. Bulk turbulence through the fluid was captured using the k–ε turbulence model with 5 % turbulence intensity at the inlet (Kato and Launder, 1993). A modified wall functions approach using Van Driest's profile was used to characterize the flow in the near-wall region (SolidWorks, 2013, 2019).

145   The domain width was 7 m and height was 8 m to achieve undisturbed flow at the edges of the domain and ensure uniform flow near the modeled gauge. The length of the domain was 18 m to allow hydrometeors to be released from a horizontal plane in the free-stream airflow ahead of the gauge (Fig. 1a, Table 1). The ground was modelled as an adiabatic frictionless wall, with horizontal wind speeds applied in 1 m s^{-1} increments from 0 to 10 m s^{-1}. A finite-volume approach with rectangular parallelepipeds for fluid cells and polyhedrons at fluid solid interfaces was used for mesh generation. Control planes were

150   centered around the gauge axis for mesh symmetry around the gauge, with the x-axis along the length of the domain in the wind direction, y-axis crosswise across the domain width, and the z-axis in the vertical direction. A clustered mesh with first-

order refinement around the gauge (8 mm cells) and secondary refinement of 2 mm cells around the mounting post, gauge, and orifice (8.3 million cells in total) was used to resolve the nonlinear updraft velocity profile around the leading edge of the gauge rim and fluid dynamics in the area of the orifice (Figs. 1c and d). The same mesh was utilized at each of the wind speeds

155 used in the analysis, with maximum y$^+$ values verified to be less than 100 at all wind speeds (Launder and Spalding, 1974;Spalding, 1961). Simulations for each of the wind speeds were run to convergence for mass, energy, and momentum with model details summarized in Table 1.

Table 1. Computational fluid dynamics and Lagrangian hydrometeor tracking model

Component	Description
Model	Favre-averaged Navier-Stokes, steady-state, k-ε, isothermal, incompressible, gravitational acceleration $a_z = $ -9.81 m s^{-2}
Fluid	Air (gas): molecular mass 0.02896 kg mol^{-1}
Boundary conditions	Ground: ideal wall (adiabatic, frictionless)
Initial and ambient conditions	$P = 101325$ Pa, $T = 293.2$ K, $u_w = 0,1,2,\ldots,10$ m s^{-1} (free-stream wind speed along x)
Domain	Length $x = 18$ m, width $y = 7$ m, height $z = 8$ m
Mesh	8.3 million cells, $y^+_{mean} = 2.5$ $y^+_{max} = 15.1$ (u_w=1 m s^{-1}), $y^+_{mean} = 17.2$ $y^+_{max} = 90.8$ (u_w=10 m s^{-1})
Hydrometeor injection	Horizontal injection rectangle: length $x = 5.5$ m, width $y = 0.4$ m, height $z = 2$ to 8 m 100000 hydrometeors/rectangle (~4.5 hydrometeors/cm^2)
Hydrometeor tracking	Lagrangian, uncoupled, spherical hydrometeors, elastic wall reflection inside gauge orifice

160
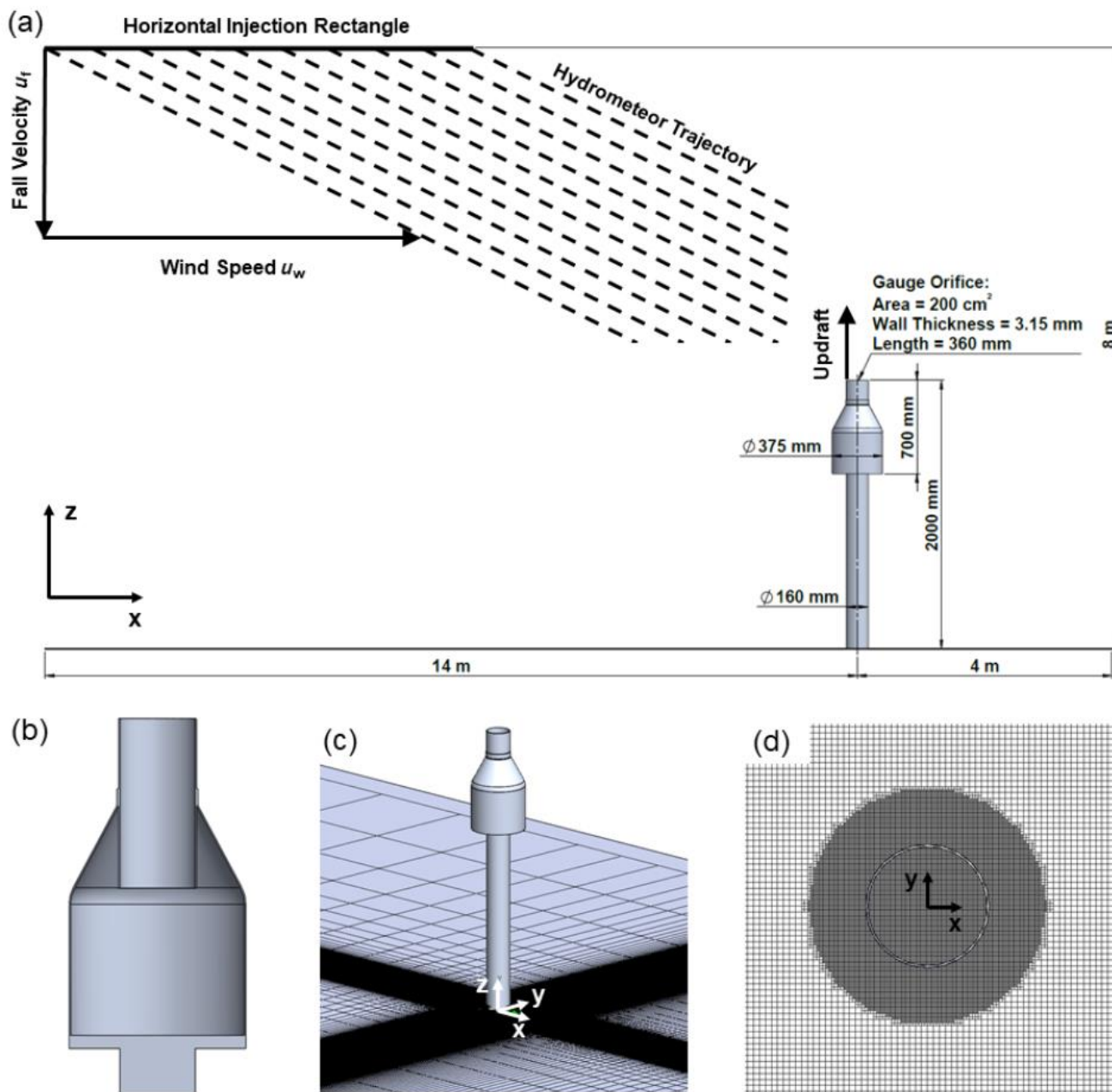
Figure 1. Unshielded Geonor T-200B3 600mm capacity gauge and model geometry, including (a) computational domain with ground, horizontal hydrometeor injection rectangle, free-stream hydrometeor trajectories based on wind speed and hydrometeor fall velocity and local updraft around leading edge of gauge orifice; (b) Geonor gauge section view; (c) clustered mesh around gauge; and (d) horizontal mesh around gauge orifice (z = 2 m).

2.2 Collection efficiency based on hydrometeor fall velocity and wind speed

For each wind speed, monodispersed hydrometeors were injected from a horizontal plane upstream and above the gauge orifice (Fig. 1a). Hydrometeor types were characterized by their fall velocity, diameter, density, and mass (Table 2). For dry snow

170 and wet snow, the hydrometeor sizes are related to the fall velocity by a general power law (Rasmussen et al., 1998). The fall velocity for dry snow u_{dry} (cm s^{-1}) is a function of the size D_{dry} (cm), with a similar relationship for wet snow (Eqs. 1a and b).

$$u_{dry} = 107 D_{dry}^{0.2},$$ (1a)

$$u_{wet} = 214 D_{wet}^{0.2},$$ (1b)

175 For dry snow and wet snow, the hydrometeor density was chosen to provide the desired hydrometeor fall velocity, with the drag coefficient for spherical hydrometeors given by Henderson (1976) based on the relative hydrometeor to air velocity. This drag formulation closely matches that of Haider and Levenspiel (1989), and has been used in previous studies (Baghapour and Sullivan, 2017).

180 **Table 2.** Characteristics for rain, dry snowflake, wet snowflake, and ice pellet hydrometeors.

Description	Diameter (m)	Density (kg m^{-3})	Mass (kg)	Fall Velocity (m s^{-1})
Rain	9.989E-05	9.982E+02	5.209E-10	0.25
Rain	1.571E-04	9.982E+02	2.028E-09	0.50
Rain	2.121E-04	9.982E+02	4.986E-09	0.75
Rain	2.671E-04	9.982E+02	9.956E-09	1.00
Rain	3.227E-04	9.982E+02	1.756E-08	1.25
Rain	3.793E-04	9.982E+02	2.851E-08	1.50
Rain	4.370E-04	9.982E+02	4.363E-08	1.75
Rain	4.962E-04	9.982E+02	6.385E-08	2.00
Rain	5.569E-04	9.982E+02	9.029E-08	2.25
Rain	6.195E-04	9.982E+02	1.242E-07	2.50
Rain	1.378E-03	9.982E+02	1.369E-06	5.00
Rain	3.956E-03	9.982E+02	3.236E-05	10.00
Dry snow	2.228E-04	5.439E+02	3.150E-09	0.50
Dry snow	1.692E-03	3.745E+01	9.498E-08	0.75
Dry snow	7.130E-03	8.837E+00	1.677E-06	1.00
Wet snow	2.228E-04	1.345E+03	7.790E-09	1.00
Wet snow	6.800E-04	3.099E+02	5.101E-08	1.25
Wet snow	1.692E-03	1.062E+02	2.693E-07	1.50
Wet snow	3.657E-03	4.728E+01	1.211E-06	1.75
Wet snow	7.130E-03	2.695E+01	5.114E-06	2.00
Wet snow	1.285E-02	1.731E+01	1.922E-05	2.25
Wet snow	2.176E-02	1.221E+01	6.586E-05	2.50
Ice pellet	1.472E-03	9.167E+02	1.532E-06	5.00
Ice pellet	4.276E-03	9.167E+02	3.752E-05	10.00

For dry snow, hydrometeor fall velocities between 0.5 m s^{-1} to 1.0 m s^{-1} were included, representing sizes up to 7 mm and densities below that of ice (Table 2). Fall velocities for wet snow were selected between 1.0 m s^{-1} to 2.5 m s^{-1} for sizes between 0.2 to 21.8 mm. Spherical ice pellets with a density of 916.7 kg/m^3 were also included in the analysis for fall velocities of 5.0 m s^{-1} and 10.0 m s^{-1}. Spherical rain hydrometeors with a density of 998.2 kg/m^3 were included for fall velocities from 0.25 m

185 s^{-1} to 10 m s^{-1} for comparison.

The hydrometeor trajectory was derived from the drag force, gravitational force, and buoyancy forces acting on the hydrometeor as it moves through the flow using Lagrangian analysis. A dilute two-phase flow was assumed, where the influence of the hydrometeors on the fluid flow was negligible and hydrometeor interactions were ignored. Combining these forces gave the net hydrometeor acceleration $\boldsymbol{a}_\mathrm{p}$ as a function of the drag coefficient C_D, hydrometeor cross sectional area

190 A_p, density of air ρ_a, relative hydrometeor to air velocity $\boldsymbol{u}_\mathrm{p} - \boldsymbol{u}_\mathrm{a}$, hydrometeor density ρ_p, hydrometeor volume V_p, and acceleration due to gravity g acting in the negative $\hat{\mathbf{z}}$ direction as shown in Eq. (2).

$$\boldsymbol{a}_\mathrm{p} = \frac{\mathrm{d}\boldsymbol{u}_\mathrm{p}}{\mathrm{d}t} = -\frac{C_\mathrm{D}\rho_\mathrm{a}A_\mathrm{p}\left|\boldsymbol{u}_\mathrm{p} - \boldsymbol{u}_\mathrm{a}\right|\left(\boldsymbol{u}_\mathrm{p} - \boldsymbol{u}_\mathrm{a}\right)}{2\rho_\mathrm{p}V_\mathrm{p}} + \frac{\left(\rho_\mathrm{a} - \rho_\mathrm{p}\right)g}{\rho_\mathrm{p}}\hat{\mathbf{z}} , \qquad (2)$$

The hydrometeors were injected into the flow with an initial velocity $\boldsymbol{u}_\mathrm{p1}$ equal to the free-stream wind speed u_w along the $\hat{\mathbf{x}}$ direction and hydrometeor fall velocity u_f in the negative $\hat{\mathbf{z}}$ direction (down).

195 $$\boldsymbol{u}_\mathrm{p1} = u_\mathrm{w}\hat{\mathbf{x}} - u_\mathrm{f}\hat{\mathbf{z}} , \qquad (3)$$

This ensured that the hydrometeors fell uniformly at equilibrium before they encountered the local flow field around the gauge. In the free-stream region under steady-state conditions, the hydrometeor fall velocity and terminal velocity will be equivalent. Hydrometeor interactions within the gauge orifice were assumed to be ideal reflections.

The collection efficiency $CE\left(u_\mathrm{w}, u_\mathrm{f}\right)$ for a given free-stream wind speed u_w and hydrometeor fall velocity u_f corresponds to

200 the ratio of the number of hydrometeors collected N_C over the horizontal gauge orifice area A_C to the number of hydrometeors injected from the horizontal injection plane above N_I over the horizontal injection plane area A_I, as shown in Eq. (4).

$$CE\left(u_\mathrm{w}, u_\mathrm{f}\right) = \frac{\dfrac{N_\mathrm{C}}{A_\mathrm{C}}}{\dfrac{N_\mathrm{I}}{A_\mathrm{I}}} = \frac{N_\mathrm{C}A_\mathrm{I}}{N_\mathrm{I}A_\mathrm{C}} , \qquad (4)$$

The horizontal injection rectangle size of 0.4 m by 5.5 m was sufficiently large to ensure a wide spread of hydrometeors over

205 the gauge orifice. The number of hydrometeors injected per unit area was high (~100000 hydrometeors/rectangle or ~4.5 hydrometeors/cm^2) to ensure high resolution of the collection efficiency estimation.

2.3 Overall collection efficiency with wind speed

The collection efficiency presented in Sect. 2.2 was for mono-dispersed hydrometeors with identical size, mass, density and fall velocity. In this section, we define the overall collection efficiency as that derived over the entire hydrometeor size distribution and associated characteristics based on observations for liquid and solid precipitation.

2.3.1 Rainfall

The total precipitation intensity P_{Total} is a function of the hydrometeor size distribution $N_R(D)$, density $\rho_{\text{p}}(D)$, volume $V_{\text{p}}(D)$, fall velocity $u_{\text{f}}(D)$, and density of water ρ_{w}.

$$P_{\text{Total}} = \frac{1}{\rho_{\text{w}}} \int_0^\infty N_R(D)\rho_{\text{p}}(D)V_{\text{p}}(D)u_{\text{f}}(D)\,\mathrm{d}D \,, \tag{5}$$

The hydrometeor size distribution (number of hydrometeors per unit size per unit volume) for raindrops $N_R(D)$ can be expressed as a gamma distribution defined by the parameter N_{0R} (m^{-3} cm$^{-1-\mu}$), exponential factor Λ_R (cm^{-1}), exponent μ (unitless), and hydrometeor diameter D (cm) as given by Ulbrich (1983).

$$N_R(D) = N_{0R}D^\mu e^{-\Lambda_R D} \,, \tag{6}$$

Assuming the product of the exponential factor and the maximum hydrometeor diameter is large, the exponential factor can be expressed in terms of the exponent and median volume diameter D_{0R} (cm).

$$\Lambda_R = \frac{3.67 + \mu}{D_{0R}} \,, \tag{7}$$

The median volume diameter is determined based on the rainfall intensity R (mm/hr) and the empirical constants ε and δ for the specific rain type.

$$D_{0R} = \varepsilon R^\delta \,, \tag{8}$$

The value of the exponent μ will be positive or negative depending on the rain type (orographic, thunderstorm, stratiform, or showers), corresponding to a concave up or down distribution when plotted on a $\log(N_R(D))$ versus D plot. Orographic rain with an exponent less than zero corresponds to a concave up distribution with small droplets and low fall speed (Ramana et al., 1959) (Table 3). Thunderstorm rain with a concave down distribution corresponds to large drops and high fall speed (Blanchard, 1953).

The hydrometeor fall velocity for rainfall is given by Beard (1976). At standard air temperature and pressure, the rainfall hydrometeor fall velocity u_{f} (m s^{-1}) is a function of the equivalent hydrometeor diameter, acceleration due to gravity g, raindrop hydrometeor density (density of water) $\rho_{\text{w}} = 1000 kg/m^3$, density of air $\rho_{\text{a}} = 1.23 kg/m^3$, dynamic viscosity of air $\eta = 1.79E-5 N \cdot s/m^2$, and surface tension of water $\sigma_{\text{w}} = 0.07199 N/m$.

Table 3. Rainfall parameters for gamma drop size distribution summarized by Ulbrich (1983).

Description	μ	N_0	ε	δ	Source
Orographic rain	-1.03	9.82 x 10^3	0.055	0.28	Ramana et al. (1959)
Thunderstorm rain	1.01	1.24 x 10^6	0.101	0.18	Blanchard (1953)

235

The overall collection efficiency is the ratio of the precipitation intensity that is captured by the gauge to that which is falling in the free-stream airflow for a given hydrometeor size distribution, following the approach of Nešpor and Sevruk (1999). The collection efficiency is implicitly dependent on the equivalent hydrometeor diameter through the hydrometeor fall velocity.

$$CE_{R,Overall} = \frac{\int_0^\infty CE(u_w, u_f) D^3 N_R(D) u_f(D) \, dD}{\int_0^\infty D^3 N_R(D) u_f(D) \, dD} , \tag{9}$$

240 **2.3.2 Snowfall**

The total precipitation intensity $P_{S,Total}$ for snowfall is a function of the hydrometeor size distribution for snowfall $N_S(D)$, density $\rho_p(D)$, volume $V_p(D)$, fall velocity $u_f(D)$ and density of water ρ_w, integrated over the range of equivalent diameters D.

$$P_{S,Total} = \frac{1}{\rho_w} \int_0^\infty N_S(D) \rho_p(D) V_p(D) u_f(D) \, dD , \tag{10}$$

245 Taking the equivalent snowfall diameter as that for a spherical water droplet with the density of water gives the total precipitation intensity integral as a function of the snowfall size distribution. Using this approach, both the size distribution and fall velocities for the snowflakes are defined as a function of the equivalent spherical diameter of water droplets.

$$P_{S,Total} = \frac{\pi}{6} \int_0^\infty D^3 N_S(D) u_f(D) \, dD , \tag{11}$$

The size distribution for snowflakes $N_S(D)$ can be expressed by the Gunn and Marshall size distribution (Gunn and Marshall,

250 1957) as a function of the size distribution parameter N_{0S} (m^{-1} mm^{-1}), exponential factor Λ_S (cm^{-1}), and equivalent spherical water drop diameters D (cm) above 0.1 cm.

$$N_S(D) = N_{0S} e^{-\Lambda_S D} , \tag{12}$$

The size distribution parameter N_{0S} (m^{-1} mm^{-1}) and exponential factor Λ_S (cm^{-1}) vary with the precipitation intensity R (mm h^{-1}).

255 $$N_{0S} = 3.8 \times 10^3 R^{-0.87} , \tag{13}$$

$$\Lambda_S = 25.5R^{-0.48}, \tag{14}$$

The median volume diameter D_{0S} (cm) varies with the size distribution slope parameter or precipitation intensity as shown by Atlas (1953).

$$D_{0S} = \frac{3.67}{\Lambda_S}, \tag{15}$$

260   The fall velocity $u_f(D)$ (cm s^{-1}) for various snowfall types, based on the equivalent spherical diameter of water droplets D (cm), is given by a general power law.

$$u_f(D) = aD^b, \tag{16}$$

The fall velocity power law coefficients for dendrites, rimed dendrites, and a mixture of dendrites and aggregates of plates is summarized in Table 4 based on the work of Langleben (1954).

265

Table 4. Snowfall fall velocity parameters with power law formulation for equivalent water droplet diameter.

Description	a	b	Source
Dendrites	178	0.372	Langleben (1954)
Rimed dendrites	210	0.283	Langleben (1954)
Mixture of dendrites and aggregate of plates	366	0.611	Langleben (1954)

The overall collection efficiency at a given wind speed is the ratio of the precipitation intensity that is captured by the gauge to that which is falling in the free-stream airflow for a given crystal habit and size distribution. As with that for rainfall, the

270   collection efficiency is implicitly dependent on the equivalent hydrometeor diameter through the hydrometeor fall velocity.

$$CE_{S,\text{Overall}} = \frac{\int_0^\infty CE(u_w, u_f)D^3 N_S(D)u_f(D)\,\mathrm{d}D}{\int_0^\infty D^3 N_S(D)u_f(D)\,\mathrm{d}D}, \tag{17}$$

3 Results

3.1 Numerical modelling

Computational fluid dynamics simulations that included the time-averaged effects of flow turbulence were run for free-stream

275   wind speeds between 0 and 10 m s^{-1} for the unshielded Geonor precipitation gauge. Results for the 1 m s^{-1} case are shown in Fig. 2. The flow is diverted upward as it passes over the leading edge of the gauge, with recirculation of the airflow within the gauge orifice (Fig. 2a). The upward z velocity profile directly above the leading edge of the gauge orifice shows a sharp

increase from zero up to a peak value of 0.95 m s^{-1} roughly 7.6 mm above the orifice, and decreases with height above this point (Fig. 2b).

280
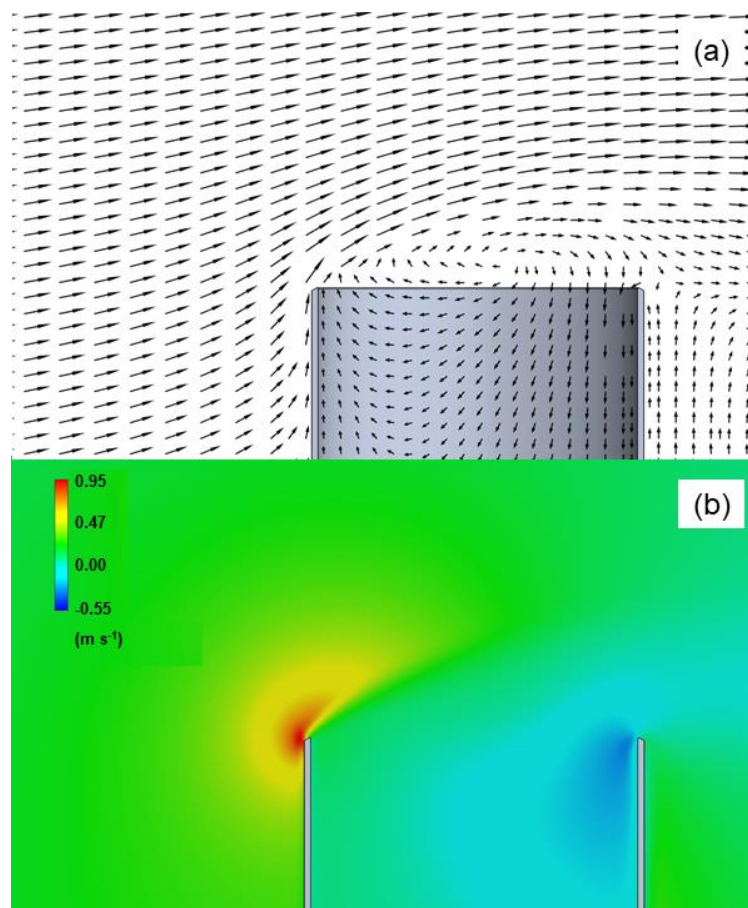
Figure 2. Air velocity around Geonor gauge for 1 m s^{-1} free-stream horizontal wind speed represented by (a) velocity magnitude and direction and (b) upward z velocity.

285   Peak velocities along the gauge centerline, normalized by the free-stream wind speed u^*, are compared with results from previous studies for wind speeds of 1 m s^{-1} and 10 m s^{-1} in Fig. 3. The peak normalized velocities are 2 % lower than the Baghapour et al. (2017) k-ω SST model at 1 m s^{-1} wind speed (Fig. 3a) and within 1 % at 10 m s^{-1} wind speed (Fig. 3b). Larger differences in peak normalized velocity, within 9 %, are observed relative to the Colli (2016a) k-ω SST model results at 1 m s^{-1} wind speed (Fig. 3a).

290
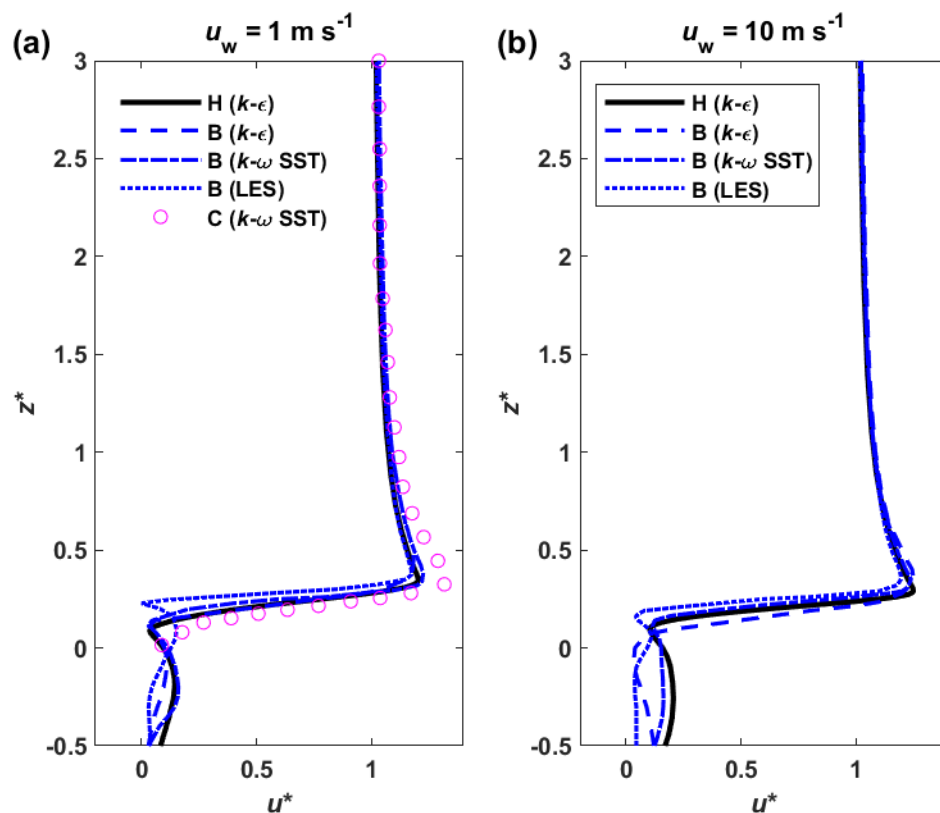
Figure 3. Gauge centerline results comparison above gauge orifice for present model (H k-ε), Baghapour et. al. (2017) k-ε model (B k-ε), Baghapour et. al. (2017) k-ω shear stress tensor model (B k-ω SST), Baghapour et. al. (2017) LES model (B LES), and Colli et. al. (2016a) k-ω shear stress tensor model (C k-ω SST) for normalized free-stream velocity with (a) 1 m s^{-1} wind speed and (b) 10 m s^{-1} wind speed.

295

For visualization purposes, hydrometeor trajectories are illustrated for the 3 m s^{-1} wind speed case with fall velocities of 0.5 m s^{-1}, 1.0 m s^{-1}, 1.5 m s^{-1} and 2.0 m s^{-1} in Fig. 4. As the fall velocity increases, the hydrometeor approach angle increases, based on the relative magnitudes of the wind speed and fall velocity. For the 2.0 m s^{-1} hydrometeor fall velocity, it is apparent that the hydrometeor trajectories experience little change due to the local airflow around the gauge (Fig. 4d). For lower fall

300 velocities, the deflection due to the updraft around the leading edge of the gauge is more apparent, with the 0.5 m s^{-1} fall velocity hydrometeors closely coupled to the flow upward and over the gauge, with a few hydrometeors drawn in at the back side of the gauge orifice (Fig. 4a). For each of the hydrometeor injections, the same horizontal spacing of hydrometeors is present prior to encountering the local airflow around the gauge. The number of hydrometeors captured is reduced for lower hydrometeor fall velocities at the same wind speed. At 3 m s^{-1} wind speed, rainfall hydrometeors with 0.25 m s^{-1} hydrometeor

305 fall velocity are all carried over the gauge, corresponding to a collection efficiency of zero (not shown).
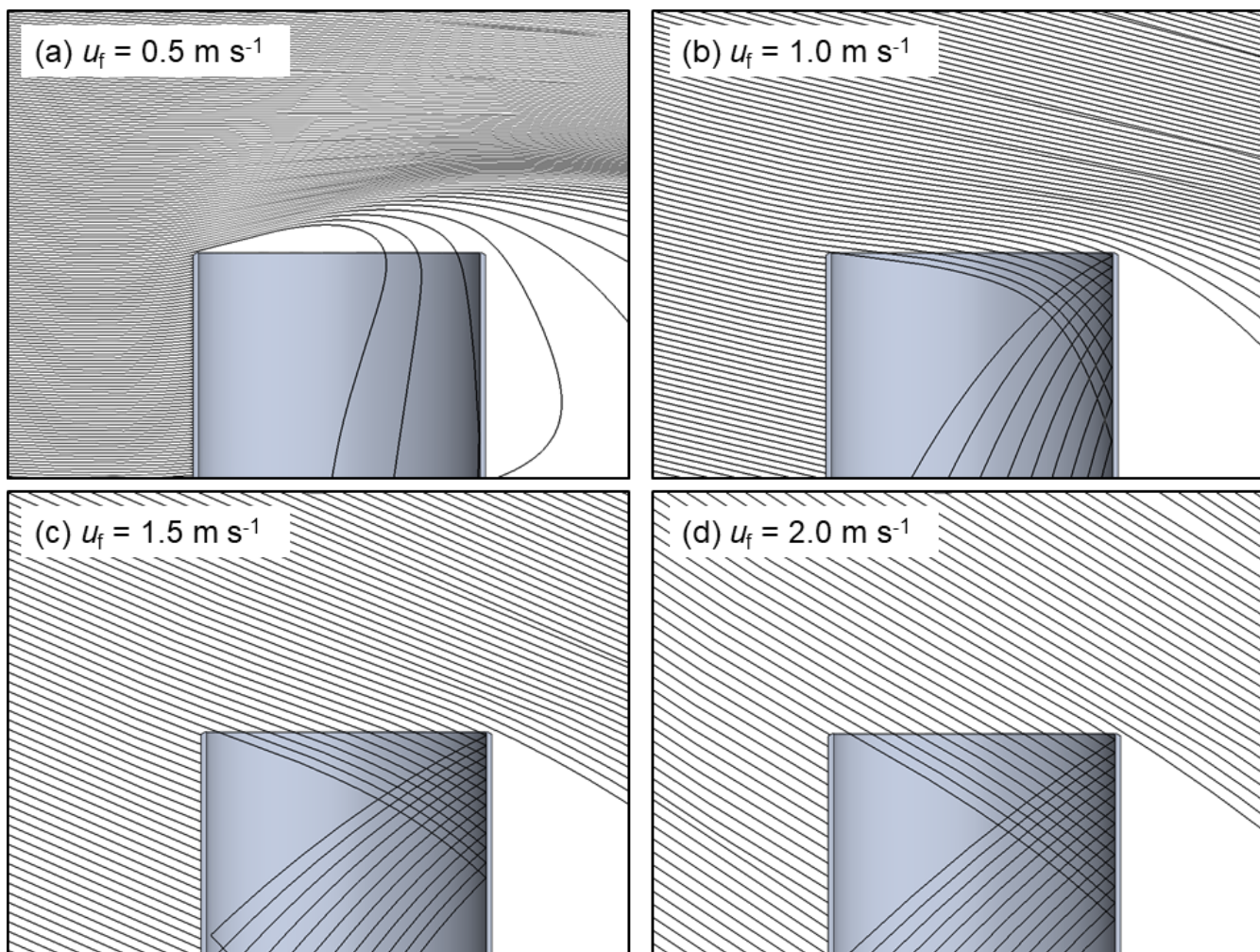
Figure 4. Flow simulation results showing hydrometeor trajectories for 3 m s⁻¹ free-stream wind velocity with rain hydrometeor fall velocity of (a) 0.5 m s⁻¹, (b) 1.0 m s⁻¹, (c) 1.5 m s⁻¹, and (d) 2.0 m s⁻¹.

310

3.2 Collection efficiency dependency on wind speed and hydrometeor fall velocity

The numerical results demonstrate a clear dependence on the hydrometeor fall velocity (Fig. 5). Hydrometeors with higher fall velocities exhibit increased collection efficiency, and the collection efficiency tends to decrease with increasing wind speed. Rain, dry snow, and wet snow hydrometeors with 1.0 m s⁻¹ fall velocity exhibit a similar collection efficiency decrease with

315   increasing wind speed, despite differences in diameter, density, and mass. For rain and ice pellet hydrometeors with 5.0 m s⁻¹ fall velocities, the results are close to 1 and nearly identical at all wind speeds, irrespective of differences in density. Rain and wet snow with identical fall velocities between 1.0 m s⁻¹ and 2.5 m s⁻¹ also exhibit similar results for wind speeds under 5 m s⁻¹. Above 5 m s⁻¹ wind speed, the collection efficiency for rain is slightly elevated above that for wet snow. For dry snow

hydrometeors with fall velocities between 0.5 m s^{-1} and 1.0 m s^{-1}, there is good agreement with the corresponding rain

320 hydrometeors up to about 3 m s^{-1} wind speed. Above this wind speed, the 0.5 m s^{-1} dry snow hydrometeors exhibit good

agreement with rain hydrometeors, while the collection efficiency for 1.0 m s^{-1} dry snow hydrometeors decreases more rapidly

with wind speed relative to rain hydrometeors with the same fall velocity. Collection efficiency differences across all

hydrometeor types with identical fall velocities are within 0.18, with root mean square differences of 0.05, over all wind speeds

and hydrometeor fall velocities studied.

325
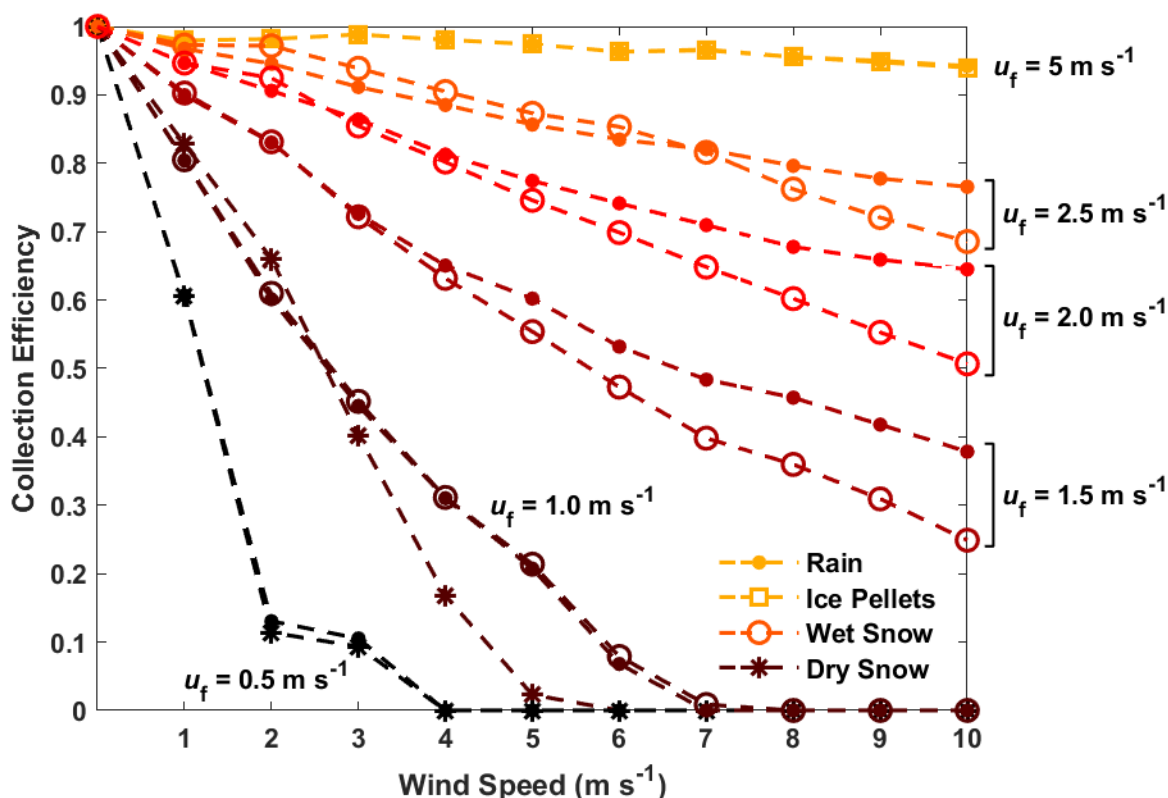
Figure 5. Flow simulation results for Geonor unshielded gauge collection efficiency based on wind speed and hydrometeor fall velocity for rain, ice pellets, wet snow, and dry snow.

330 **3.3 Empirical collection efficiency expression**

The simulation results demonstrate that the collection efficiency is dependent on the free-stream wind speed u_w and

hydrometeor fall velocity u_f. An empirical expression for the collection efficiency $CE(u_w, u_f)$ is presented based on a

polynomial fit to wind speed and an exponential hydrometeor fall velocity dependence, with both velocities having units of m s^{-1}.

$$CE\left(u_{\mathrm{w}}, u_{\mathrm{f}}\right) = 1 - b_1 u_{\mathrm{w}} e^{-b_2 u_{\mathrm{f}}} + b_3 u_{\mathrm{w}}^2 e^{-b_4 u_{\mathrm{f}}} , \tag{18}$$

This expression was selected due to its ability to capture the nonlinearity in the collection efficiency up to 10 m s^{-1} wind speed, as well as the nonlinear fall velocity dependence with collection efficiencies approaching 1 for higher fall velocities. Table 5 shows the best-fit coefficients (RMSE of 0.03) from a combined nonlinear regression for dry snow (0.5 m s^{-1} and 0.75 m s^{-1} fall velocities), wet snow (1.0 m s^{-1}, 1.25 m s^{-1}, ... , 2.5 m s^{-1} fall velocities), and rain (5 and 10 m s^{-1} fall velocities).

Table 5. Non-linear regression fit parameters, standard errors (SE), and units for the Geonor unshielded gauge collection efficiency as a function of wind speed and hydrometeor fall velocity with RMSE = 0.0302 and R^2 = 0.989.

Coefficient	Value	SE	Units
b_1	0.908	0.048	s m^{-1}
b_2	1.387	0.037	s m^{-1}
b_3	0.143	0.031	s^2 m^{-2}
b_4	2.422	0.167	s m^{-1}

A wind speed threshold u_{wc} is defined above which the collection efficiency is zero for a given maximum cutoff hydrometeor fall velocity u_{fc}. This was derived from Eq. (18) by solving for the roots where the collection efficiency is zero using the quadratic formula. Conversely, this expression gives the hydrometeor fall velocity below which the collection efficiency will be zero for a given wind speed.

$$u_{\mathrm{wc}} = \frac{b_1}{2b_3} \exp\left[\left(b_4 - b_2\right)u_{\mathrm{fc}}\right] - \frac{\sqrt{b_1^2 \exp\left(-2b_2 u_{\mathrm{fc}}\right) - 4b_3 \exp\left(-b_4 u_{\mathrm{fc}}\right)}}{2b_3 \exp\left(-b_4 u_{\mathrm{fc}}\right)} , \tag{19}$$

Fig. 6 shows a comparison of the results from the empirical expression with the CFD results. For hydrometeor fall velocities above 5.0 m s^{-1}, the collection efficiency is slightly over predicted (up to 0.05) by the expression. For fall velocities between 1.0 to 2.5 m s^{-1}, the fit is within ±0.06 over all wind speeds. For fall velocities of 0.5 m s^{-1}, the fit captures the rapid decrease in collection efficiency with wind speed well, with a maximum difference of 0.15 at 2 m s^{-1} wind speed.
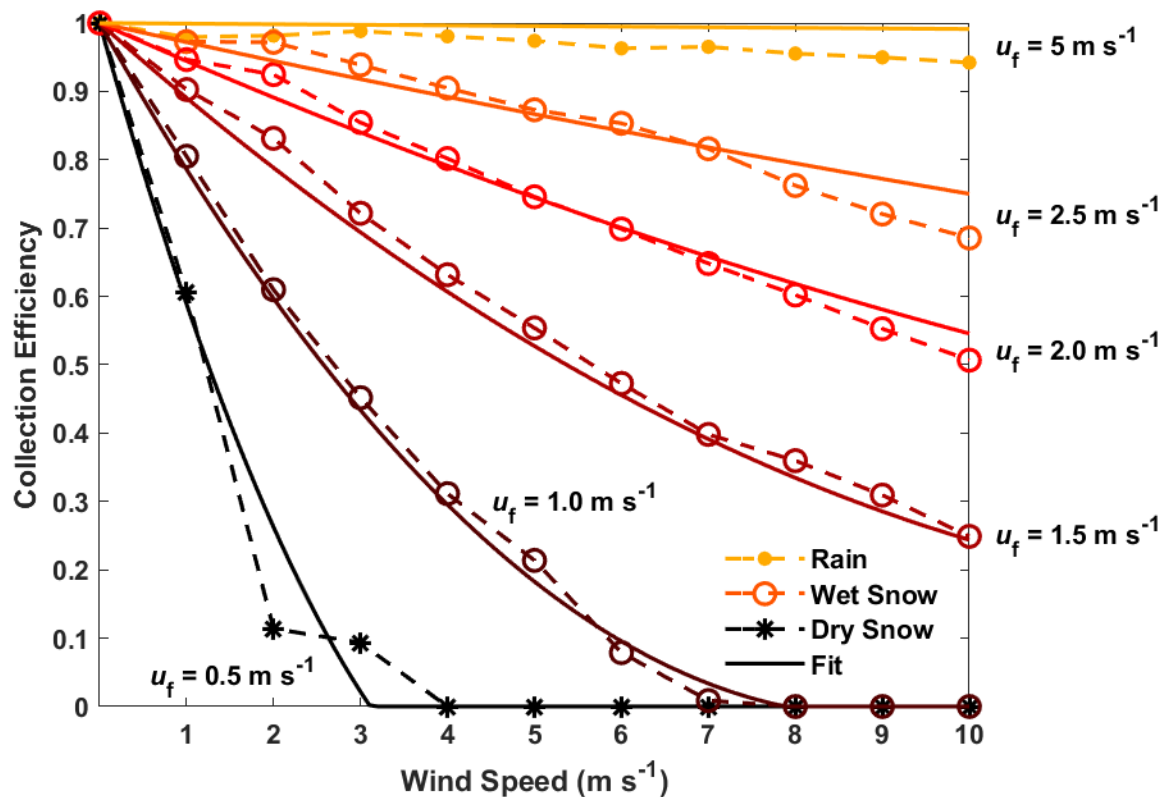
Figure 6. Geonor unshielded gauge collection efficiency results for rain, wet snow, dry snow, and exponential fit model based on wind speed and hydrometeor fall velocity.

Fig. 7 shows the empirical collection efficiency expression dependence with fall velocity. For a given wind speed, the collection efficiency increases nonlinearly with hydrometeor fall velocity. For fall velocities above 3 m s^{-1} the collection efficiency is close to 1. The collection efficiency rapidly decreases as the fall velocity is reduced, particularly below 2.5 m s^{-1} fall velocity. Increasing the wind speed decreases the collection efficiency. The fall velocity where the collection efficiency is zero illustrates the fall velocity cutoff given by Eq. (19). Hydrometeors at or below this fall velocity will not be captured by the gauge. As the wind speed increases, the fall velocity cutoff increases, reaching 1.1 m s^{-1} at 9 m s^{-1} wind speed.
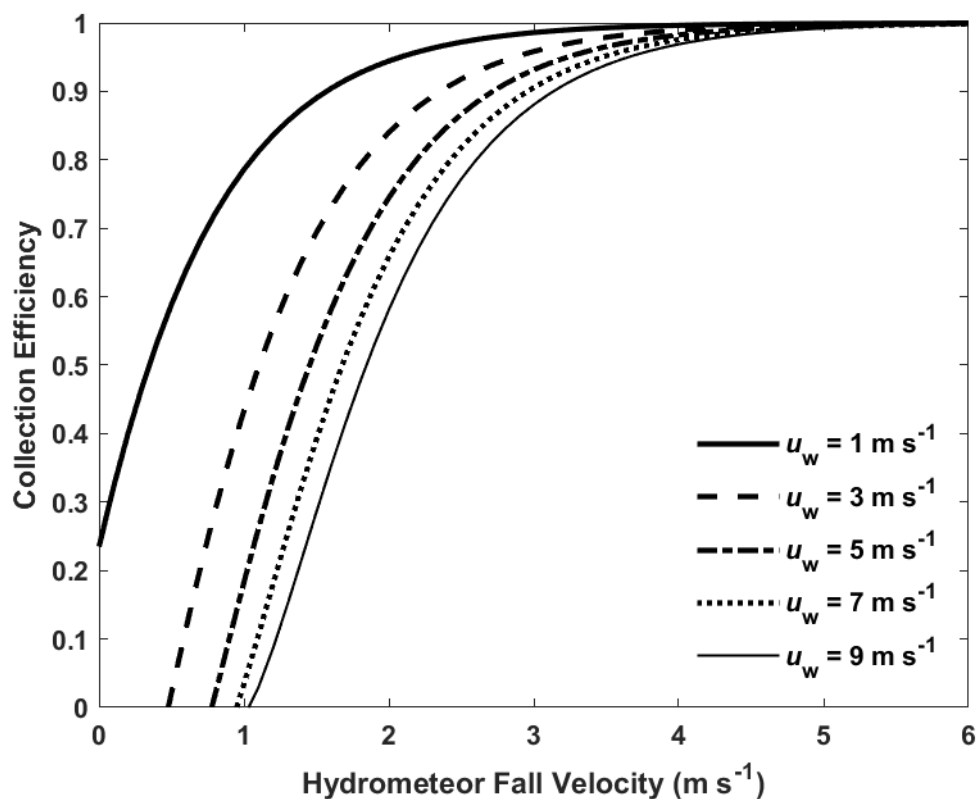
Figure 7. Geonor unshielded gauge collection efficiency for exponential fit model with hydrometeor fall velocity and wind speed.

3.4 Overall collection efficiency

3.4.1 Comparison with previous studies

370   The overall collection efficiency for a distribution of hydrometeors is obtained by integrating the ratio of the precipitation intensity captured by the gauge to that which is falling in air over the range of hydrometeor sizes present. The empirical expression (Eq. 18) captures the gauge collection efficiency for a given wind speed and hydrometeor fall velocity. A hydrometeor size distribution with intercept $N_{0S} = 5 \times 10^6 \, \text{m}^{-4}$ and slope $\Lambda_S = 1 \text{mm}^{-1}$ for hydrometeor sizes between 0.25 mm to 20 mm was used for dry snow and wet snow for comparison with the work of Colli et al. (2016b). Overall collection

375   efficiency results between the two models show good agreement (Fig. 8). For dry snow, the overall collection efficiency decreases more gradually with wind speed in the present study than the Colli et al. (2016b) results, with collection efficiency values up to 0.18 higher at 3 m s^{-1} wind speed using the present model. For wet snow, the results of Colli et al. (2016b) show a nonlinear decrease in collection efficiency above 5 m s^{-1} wind speed that is not apparent in the results from the present study. As a result, the present study predicts up to 0.16 higher collection efficiency at 8 m s^{-1} wind speed.
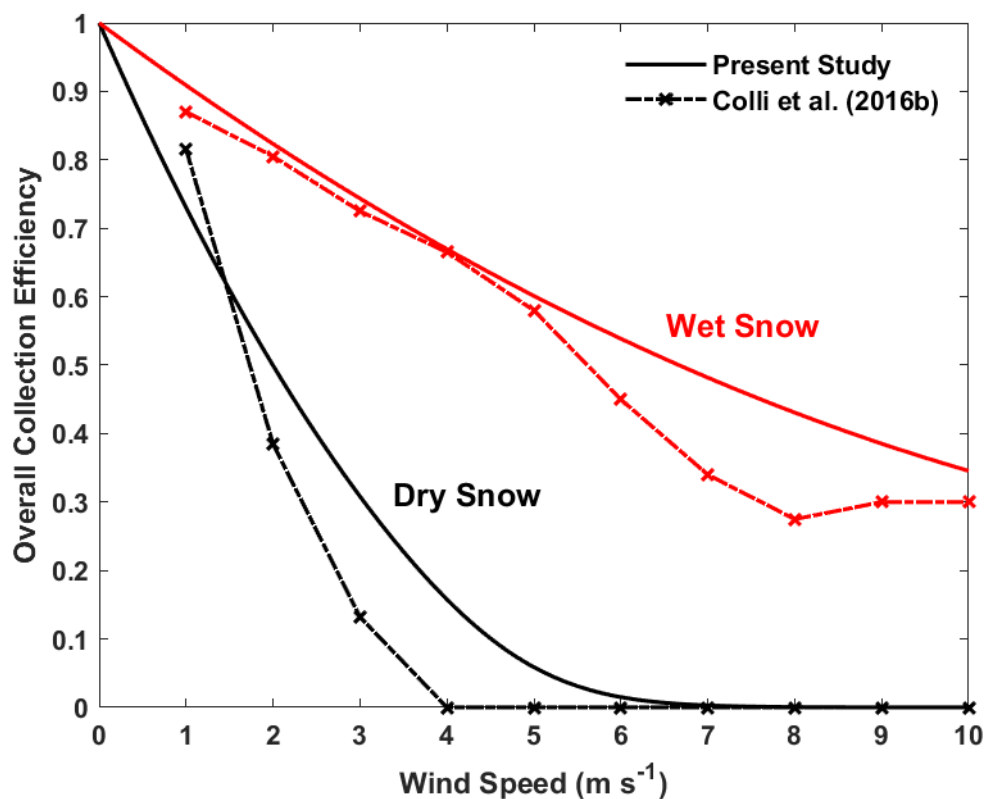
Figure 8. Overall Geonor unshielded gauge collection efficiency with wind speed for present study and Colli et al. (2016b) k-ω SST model for dry snow and wet snow with Colli et al. (2016b) size distribution.

3.4.2 Wind speed dependence

385   For each hydrometeor type and precipitation intensity, the overall collection efficiency was derived for wind speeds from 0 to 10 m s^{-1} using the empirical expression for collection efficiency (Eq. 18) based on wind speed and hydrometeor fall velocity. The collection efficiency decreases nonlinearly with wind speed, decreasing more rapidly at lower wind speeds and more gradually at higher wind speeds above approximately 5 m s^{-1} (Fig. 9). A wide range of overall collection efficiency results with wind speed is apparent, depending on the hydrometeor type and precipitation intensity.
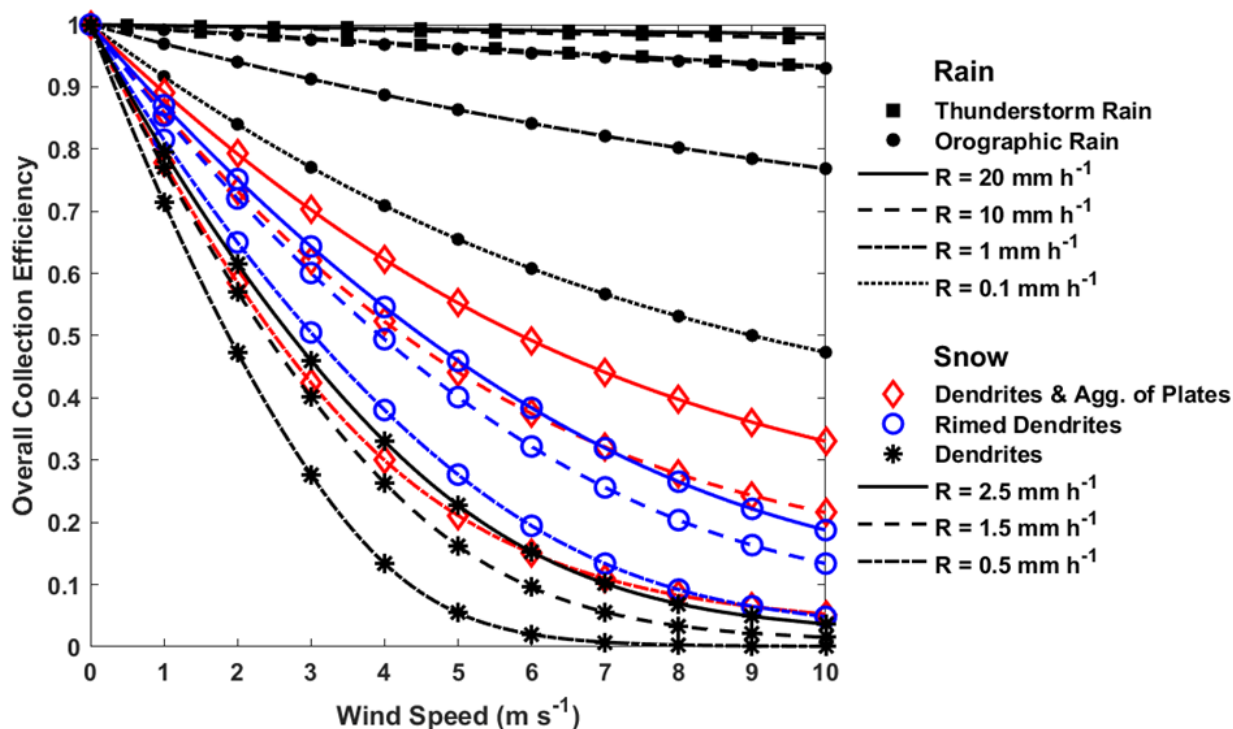
Figure 9. Overall Geonor unshielded gauge collection efficiency with wind speed for thunderstorm rain at 20 mm h^{-1}, 10 mm h^{-1}, and 1 mm h^{-1} precipitation intensities (R); orographic rain at 10 mm h^{-1}, 1 mm h^{-1}, and 0.1 mm h^{-1} precipitation intensities (R); and aggregates of plates, rimed dendrites, and dendrites at 2.5 mm h^{-1}, 1.5 mm h^{-1}, and 0.5 mm h^{-1} precipitation intensities (R).

395   Lower overall collection efficiencies are observed for snowfall relative to rain. The overall collection efficiency for dendrites with 0.5 mm h^{-1} precipitation intensity decreases to 0.01 at 6.7 m s^{-1} wind speed, exhibiting the lowest overall collection efficiency and greatest nonlinearity with wind speed. The overall collection efficiency continues to decrease with increasing wind speed, remaining small, but non-zero, up to 10 m s^{-1} wind speed. For 1.5 mm h^{-1} and 2.5 mm h^{-1} intensities, overall collection efficiencies are higher, with the magnitude of the increase varying with the wind speed.

400   Across snowfall types, a wide range of overall collection efficiency values are apparent. Dendrites show the lowest overall collection efficiency, while dendrites and aggregates of plates with 2.5 mm h^{-1} precipitation intensity show a much higher overall collection efficiency of 0.55 at 5 m s^{-1} wind speed. Dendrites and aggregates of plates also show the largest spread in overall collection efficiency with precipitation intensity, with the overall collection efficiency between 0.21 and 0.55 for 0.5 mm h^{-1} and 2.5 mm h^{-1} precipitation intensities, respectively, at 5 m s^{-1} wind speed. This spread decreases at higher wind

405   speeds as the overall collection efficiency for 0.5 mm h^{-1} decreases more gradually. Rimed dendrites provide intermediate values, above those for dendrites and below those for dendrites and aggregates of plates, for 2.5 mm h^{-1} precipitation intensity. Orographic and thunderstorm rain exhibit overall collection efficiencies greater than those for snow. The overall collection efficiencies for orographic rain at 5 m s^{-1} wind speed and 0.1 mm h^{-1}, 1 mm h^{-1} and 10 mm h^{-1} precipitation intensities are 0.66,

0.86, and 0.96, respectively. For thunderstorm rain at 5 m s⁻¹ wind speed, the overall collection efficiencies are 0.96, 0.98, and

410 0.99 at 1 mm h⁻¹, 10 mm h⁻¹, and 20 mm h⁻¹ precipitation intensities, respectively.

3.4.3 Precipitation intensity dependence

The overall collection efficiency was derived for each precipitation type, precipitation intensity, and wind speed (1 m s⁻¹, 3 m

s⁻¹, and 6 m s⁻¹). Fig. 10 shows how the overall collection efficiency varies with precipitation intensity for given wind speeds

and hydrometeor types. Overall collection efficiencies were derived for 0.5 mm h⁻¹, 1.5 mm h⁻¹, and 2.5 mm h⁻¹ precipitation

415 intensities for three different snowfall types, between 0.1 mm h⁻¹ and 10 mm h⁻¹ for orographic rain, and between 1 mm h⁻¹ and

10 mm h⁻¹ for thunderstorm rain.
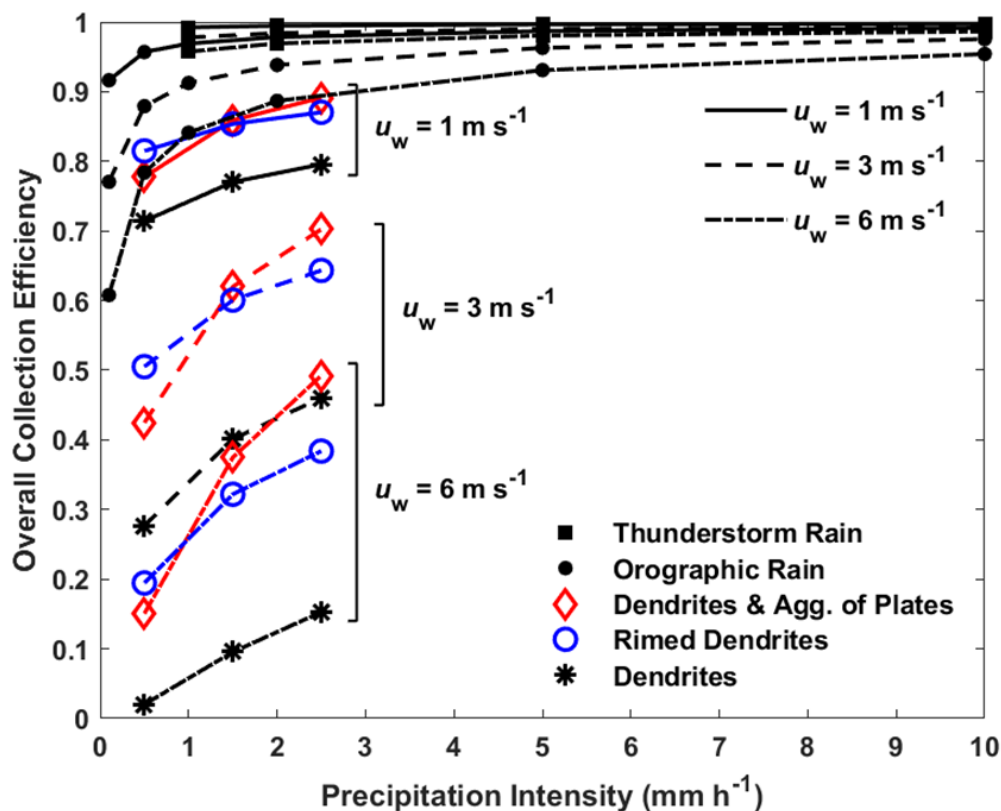
Figure 10. Overall Geonor unshielded gauge collection efficiency with precipitation intensity for rainfall and snowfall types at 1 m s⁻¹, 3 m
420 s⁻¹, and 6 m s⁻¹ wind speeds.

Overall collection efficiencies increase with precipitation intensity and decrease with wind speed. For thunderstorm rain at 3

m s⁻¹ wind speed, the overall collection efficiency increases from 0.97 to 0.99 when the precipitation intensity increases from

1 mm h⁻¹ to 10 mm h⁻¹. For orographic rain, a sharp decrease in the overall collection efficiency is apparent with decreasing

425   precipitation intensity below 1 mm h^{-1}. At 3 m s^{-1} wind speed, the overall collection efficiency for orographic rain increases
from 0.77 at 0.1 mm h^{-1}, to 0.91 at 1 mm h^{-1}, and 0.97 at 10 mm h^{-1}. Increasing the wind speed reduces the overall collection
efficiency, with the value for orographic rain decreasing from 0.97 at 1 m s^{-1} wind speed, to 0.91 at 3 m s^{-1} wind speed, and
0.84 at 6 m s^{-1} wind speed.

For all snowfall types, the overall collection efficiency is shifted to lower values relative to rain. The overall collection
430   efficiency is 0.62, 0.60, and 0.40 for dendrites and aggregates of plates, rimed dendrites, and dendrites at 3 m s^{-1} wind speed
and 1.5 mm h^{-1} precipitation intensity, respectively. The overall collection efficiency increases with precipitation intensity
from 0.42 at 0.5 mm h^{-1} to 0.70 at 2.5 mm h^{-1} for dendrites and aggregates of plates at 3 m s^{-1} wind speed. Increasing the wind
speed to 6 m s^{-1} further decreases the overall collection efficiency from 0.15 at 0.5 mm h^{-1} to 0.49 at 2.5 mm h^{-1}.

For dendrites and aggregates of plates, rimed dendrites, and dendrites, overall collection efficiencies are within 0.09 to 0.10 of
435   one another for 0.5 mm h^{-1} precipitation intensities at 1 m s^{-1} wind speed. This range increases to 0.17 for 0.5 mm h^{-1}
precipitation intensity and 0.34 for 2.5 mm h^{-1} precipitation intensity at 6 m s^{-1} wind speed. This provides an estimate of the
overall variability in collection efficiency due to crystal habit if the precipitation intensity, wind speed, and the occurrence of
snowfall are all known, but not the specific snowfall type. In cases where only the precipitation intensity and wind speed is
known, and the hydrometeor phase (rainfall or snowfall) and type is uncertain, the range of possible overall collection
440   efficiencies grows dramatically. For example, at 6 m s^{-1} wind speed, the overall collection efficiencies for rain exceed 0.75,
while that for dendrites is below 0.16; hence, the catch efficiency in this case can vary by ~ 0.74 depending on the hydrometeor
phase and type.

3.4.4 Hydrometeor fall velocity dependence

Fig. 11 shows the overall collection efficiency as a function of hydrometeor fall velocity for each precipitation type
445   (thunderstorm rain, orographic rain, dendrites and aggregates of plates, rimed dendrites, and dendrites), precipitation intensity
(0.1 to 20 mm h^{-1} for rainfall and 0.5 to 2.5 mm h^{-1} for snowfall), and wind speed (1 m s^{-1}, 3 m s^{-1}, and 6 m s^{-1}) shown previously
in Fig. 10. Here, the fall velocity at the median volume diameter is used as an estimate for the fall velocity distribution. The
results take a similar form to that of the empirical expression for collection efficiency shown in Fig. 7, with collection
efficiencies increasing nonlinearly with hydrometeor fall velocity for a given wind speed. Dendrites, with the lowest fall
450   velocity, exhibit the lowest overall collection efficiency. Rimed dendrites and dendrites and aggregates of plates with higher
fall velocity exhibit higher collection efficiency. In this fall velocity range below 1.5 m s^{-1}, the collection efficiency rapidly
increases approximately linearly with fall velocity. For orographic rain and thunderstorm rain, with even higher fall velocity,
the overall collection efficiency nonlinearly approaches 1. As wind speeds increase from 1 m s^{-1} to 6 m s^{-1}, collection
efficiencies for all precipitation types are shifted down at the lower end of the fall velocity spectrum below 2 m s^{-1} and still
455   converge to 1 at higher fall velocities, close to 5 m s^{-1}.
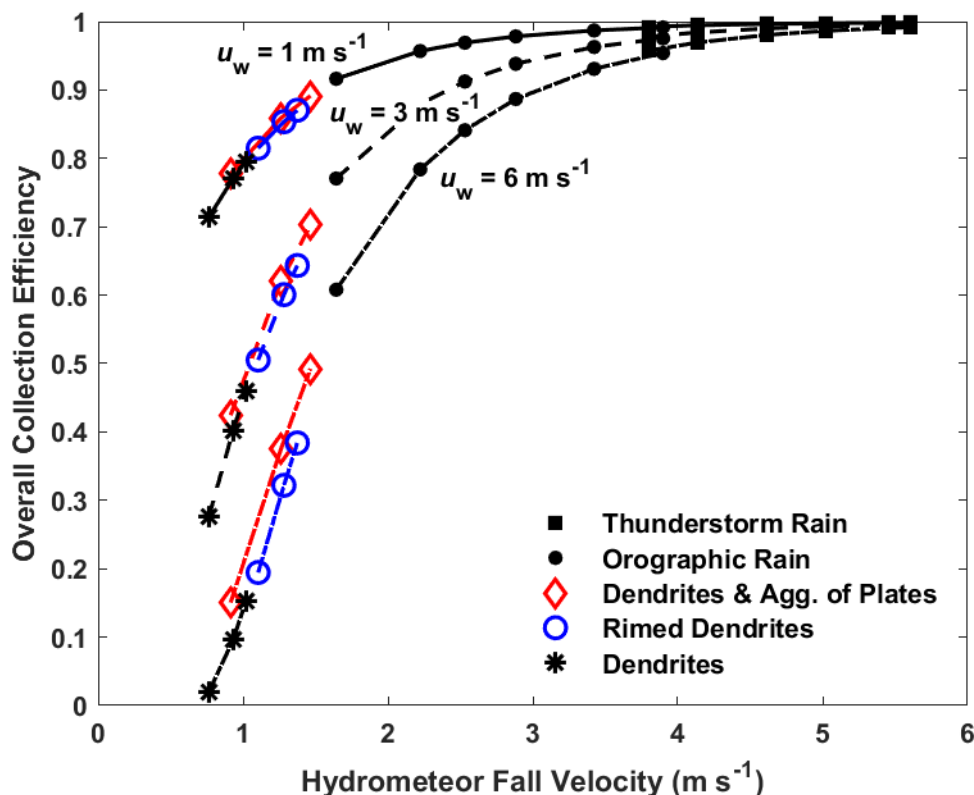
Figure 11. Overall Geonor unshielded gauge collection efficiency with hydrometeor fall velocity at median volume diameter for rainfall and snowfall types at 1 m s^{-1}, 3 m s^{-1}, and 6 m s^{-1} wind speeds.

460 For snowfall, the overall collection efficiency difference across dendrites, rimed dendrites, and dendrites and aggregates of plates is less than 0.06 for 0.5 mm h^{-1}, 1.5 mm h^{-1}, and 2.5 mm h^{-1} precipitation intensities at 6 m s^{-1} wind speed, and within 0.03 for the same precipitation intensities at 3 m s^{-1} wind speed. For rainfall, the overall collection efficiency difference is less than 0.01 at 3.8 m s^{-1} fall velocity, where orographic rain and thunderstorm rain overlap. Orographic rain exhibits median volume diameter fall velocities between 1.6 m s^{-1} to 3.9 m s^{-1} for precipitation intensities from 0.1 mm h^{-1} to 10 mm h^{-1}.

465 Thunderstorm rain exhibits median volume diameter fall velocities between 3.8 m s^{-1} to 5.6 m s^{-1} for precipitation intensities from 1 mm h^{-1} to 20 mm h^{-1}.

4 Discussion

4.1 Numerical modelling results

The time-averaged numerical model describes the three-dimensional airflow around the unshielded Geonor gauge, including

470 the updraft above the leading edge of the gauge orifice and downdraft at the back of the gauge orifice shown in previous studies

(Thériault et al., 2012;Colli et al., 2016a;Baghapour et al., 2017). The updraft velocity increases sharply with height above the leading edge of the gauge orifice, which appears to play an important role in the horizontal spreading and capture of hydrometeors, particularly for lower fall velocity hydrometeors (Figs. 2 and 3). These velocities scale with the wind speed, as shown previously by Colli et al. (2016a), and the relative magnitudes of the wind speed and hydrometeor fall velocity influence

475   the collection efficiency. The hydrometeor fall velocity influences the free-stream approach angle of hydrometeors before they encounter the local airflow around the gauge and the degree of coupling between the hydrometeor trajectories and the local airflow. Hydrometeors with fall velocities above 2 m s^{-1} fall more vertically, and their paths shows less deviation with the updraft and local airflow around the gauge orifice (Fig. 4). Hydrometeors with lower fall velocities have a smaller approach angle and are more closely coupled to the local airflow around the gauge orifice.

480   Normalized velocities along the gauge centerline in the present study show good agreement with the *k-w* SST simulation results of both Colli et al. (2016a) and Baghapour et al. (2017), as shown in Fig. 3. Peak normalized velocities show very good agreement with Baghapour et al. (2017) *k-ω* SST simulation results, which used a similar refined orifice thickness as that in the present study. Reductions in the peak gauge centerline velocity relative to the results from Colli (2016b) in Fig. 3 may result from refinements in the gauge geometry used in the present study, including the orifice thickness. This reasoning is

485   supported by Sevruk et al. (1994), who demonstrated that reductions in the orifice thickness can reduce the wind speed over the gauge. The sensitivity of simulation results to the model geometry is discussed in greater detail by Baghapour et al. (2017) and is an area for future study.

4.2 Collection efficiency based on wind speed and hydrometeor fall velocity

The numerical model, which captures the three-dimensional airflow and hydrometeor kinematics (assuming a spherical drag

490   model), exhibits a nonlinear reduction in collection efficiency with increasing wind speed and decreasing hydrometeor fall velocity (Fig. 5). A slight nonlinearity in the collection efficiency relationship with wind speed is apparent, with the collection efficiency decreasing more rapidly at lower wind speeds and more gradually at higher wind speeds. This wind speed dependence has been demonstrated in previous studies (Nešpor and Sevruk, 1999;Thériault et al., 2012;Colli et al., 2016a;Baghapour et al., 2017), and is generally attributed to the three-dimensional velocity profile around the gauge

495   influencing the trajectories and catchment of incoming hydrometeors.

The present study demonstrates a strong nonlinear dependence on the hydrometeor fall velocity, as well. Hydrometeors with fall velocities above 5 m/s exhibit collection efficiencies close to 1, while lower hydrometeor fall velocities influence the rate of decrease of collection efficiency with wind speed (Figs. 6 and 7). Collection efficiency decreases are most pronounced below 2.0 m/s hydrometeor fall velocity, where a wide range of collection efficiencies are possible. This demonstrates the

500   challenge in adjusting liquid, solid, and mixed precipitation accumulations in situations where different hydrometeor types and sizes – and with very different fall velocities – can occur. These findings support the conclusions of Thériault et al. (2012), who demonstrated large collection efficiency differences across dry snow and wet snow hydrometeors with different terminal

velocities. The present findings also support those of Nešpor and Sevruk (1999), who showed that the wind-induced error increases rapidly for smaller raindrop sizes with lower terminal velocities.

505   Across rain, ice pellets, wet snow, and dry snow, the numerical collection efficiency results are very similar for hydrometeors with the same fall velocity, despite differences in characteristics (size, density, and mass), as shown in Fig. 5. Rain and ice pellets, with identical fall velocities, show very good agreement in collection efficiency results with over all wind speeds. Collection efficiencies for rain and wet snow display good agreement up to approximately 4 m s^{-1} wind speed, above which collection efficiencies for rain are slightly higher than those for wet snow. This may be due to the higher density of the rain

510   hydrometeors relative to the wet snow hydrometeors, with hydrometeor inertia playing a role at higher wind speeds. At 1.0 m s^{-1} fall velocity, dry snow and wet snow hydrometeors display similar collection efficiencies up to 3 m s^{-1} wind speed. Above this wind speed, the collection efficiency for dry snow decreases more rapidly than that for wet snow and rain. Conversely, rain and dry snow hydrometeors with lower fall velocities (0.5 and 0.75 m s^{-1}) have similar collection efficiencies for all wind speeds.

515   Collection efficiency differences between 1.0 m s^{-1} dry snow and wet snow hydrometeors for wind speeds above 3 m s^{-1} may also be related to hydrometeor inertia, as the density of wet snow is approximately 150 times greater than that for dry snow at this fall velocity, as shown in Table 2. A similar rapid decrease in collection efficiency for dry snow has been demonstrated by Colli (2016b), with the collection efficiency decreasing to 0.35 at 3 m s^{-1} wind speed. This decrease may be due to the limitations of the spherical hydrometeor model; further investigation is recommended as an area for future work.

520   Hydrometeors exhibit a wide variety of habits, sizes, shapes, and densities, influencing their aerodynamics and, in turn, their ability to be captured by the gauge. The present study, using a spherical drag model, demonstrates that collection efficiencies are similar for different hydrometeor types with different sizes, densities, masses, and drag values, but similar fall velocities. This enables the characterization of collection efficiency independent of hydrometeor type, diameter, density and drag, which allows for the broad application of the transfer function in the present study to various hydrometeor types. Assessment using

525   non-spherical drag models is considered to be an area for future work.

4.3 Empirical collection efficiency expression

The empirical expression presented in Eq. 18 with a single set of coefficients (Table 5) is based on the computational fluid dynamics results for an unshielded Geonor T-200B3 600 mm capacity precipitation gauge for wind speeds up to 10 m s^{-1}. This expression provides a straightforward means of estimating the collection efficiency based on the wind speed and hydrometeor

530   fall velocity. In operational monitoring networks, the hydrometeor fall velocity can be provided by disdrometers (Loffler-Mang and Joss, 2000;Sheppard and Joe, 2000;Bloemink and Lanzinger, 2005;Nitu et al., 2018), vertically pointing Doppler radars (Biral, 2019), or multi-frequency radar techniques (Kneifel et al., 2015). Assessment of these techniques for the measurement of hydrometeor fall velocity is an area for future work.

The empirical expression captures well the nonlinear change in collection efficiency with wind speed and hydrometeor fall

535   velocity that is observed in the numerical model results (Fig. 6). This expression was derived from simulation results up to 10

m s^{-1} wind speed and should be used with caution at higher wind speeds. Application to other gauge or shield combinations should also be investigated, as the flow dynamics around the gauge orifice are dependent on the specific gauge and shield geometry.

The fall velocity cutoff, shown in Fig. 7, corresponds to the fall velocity below which no hydrometeors are captured by the

540 gauge for a given wind speed. In this case, the hydrometeors are unable to pass through the updraft region and local airflow around the gauge orifice to be captured by the gauge. As the wind speed increases, the fall velocity cutoff increases, as it becomes more difficult for hydrometeors to overcome the updraft velocity and local airflow and be captured. This has important consequences for the overall gauge collection efficiency, as hydrometeors below the fall velocity cutoff in the drop size distribution do not contribute to the total catchment. This finding agrees with the results of Nešpor and Sevruk (1999),

545 who estimated the drop diameter below which the collection efficiency is zero for rain. The present formulation based on the fall velocity can be applied more broadly across rain and snow types for the unshielded Geonor gauge configuration.

4.4 Overall collection efficiency results

4.4.1 Comparison with previous studies

The collection efficiency results using the empirical expression developed in the present study show good overall agreement

550 with the results of Colli et al. (2016b) for wet snow and dry snow, as shown in Fig. 8. Collection efficiency values in the present study are slightly higher than those of Colli et al. (2016b), who demonstrated that their model results for dry snow slightly underpredict experimental results for temperatures below -4 °C. Differences between the two models may be due to differences in the gauge geometry and hydrometeor drag model, among other factors. The gauge geometry in the present study includes a refined orifice wall thickness and full-length orifice extending down into the gauge housing (Figs. 1a and b). The

555 peak velocities above the gauge in the present study are similar to those observed by Baghapour et al. (2017), who also used a refined orifice wall thickness and observed reduced peak velocities compared to the results of Colli et al. (2016b) as discussed in Sect. 4.1. Increases in the velocity magnitude over the gauge would be expected to decrease the collection efficiency in a manner similar to that for increased wind speed; hence, the higher peak velocities above the gauge in the results of Colli et al. (2016b) provide one explanation for the lower collection efficiency values observed.

560 Differences in the hydrometeor drag model may also contribute to differences in results among the two studies. The present study uses a spherical drag model similar to that used by Baghapour and Sullivan (2017), in which the drag coefficient varies based on the relative hydrometeor-to-air velocity over the path of the hydrometeor. The results of Colli et al. (2016b) are based on a constant drag model with a fixed drag coefficient over the hydrometeor path, following the approach of Thériault et al. (2012). Both Colli et al. (2015) and Baghapour and Sullivan (2017) showed that the constant drag model can overestimate the

565 hydrometeor drag relative to empirical models, thereby reducing the collection efficiency.

The injection of hydrometeors from a horizontal plane in the present study ensures identical horizontal particle densities for each wind speed simulation following the approach of Nešpor and Sevruk (1999) for rain and Baghapour and Sullivan (2017)

for snow. Injecting hydrometeors from a vertical plane, as done in previous studies (Thériault et al., 2012;Colli et al., 2016b), could lead to reduced horizontal particle densities and less certainty in numerical collection efficiency estimates for high wind

570   speeds if the injection densities are not sufficiently high.

The present study defines the overall collection based on the ratio of precipitation rate or mass flux of precipitation captured by the gauge to that falling in air following the approach of Nešpor and Sevruk (1999). This provides a consistent formulation for collection efficiency across rainfall and snowfall types. The collection efficiency defined by Colli et al. (2016b) for wet snow and dry snow is based on a 'volumetric' approach, with the fall velocity term in the integrand omitted. Omitting the fall

575   velocity neglects the contribution of the rate of fall of hydrometeors to the overall precipitation rate, with higher fall velocities providing a greater precipitation rate. For the dry snow and wet snow comparison shown in Fig. 8 the differences between these two approaches are small.

The use of a continuous collection efficiency expression with wind speed and fall velocity dependence enables the derivation of overall collection efficiencies over intermediate sizes and fall velocities in the hydrometeor size distribution. Collection

580   efficiencies can be computed at intermediate wind speed values using this approach as well, providing the smooth overall collection efficiency curves shown in Fig. 8. Nešpor and Sevruk (1999) used a similar empirical approach for rain by developing an expression for the partial wind-induced error based on free-stream velocity and drop diameter applicable to Mk2, Hellman and ASTA gauges. The overall collection efficiency results of Colli et al. (2016b) were derived directly from numerical CE results for dry snow and wet snow at discrete sizes and wind speeds.

585   **4.4.2 Wind speed dependence**

The fall velocities of snowflakes are smaller than those of raindrops; accordingly, the collection efficiency for snowfall at a given wind speed is lower than that for rainfall (Fig. 9). Dendrites have lower fall velocities than rimed dendrites and columns and plates, and hence, have reduced ability to be collected. This results in a lower collection efficiency for dendrites relative to the other crystal types. For a precipitation intensity of 0.5 mm h^{-1}, the overall collection efficiency for dendrites remains

590   very small above 7 m s^{-1} wind speed, as only a small number of hydrometeors have sufficient fall velocity to be captured by the gauge.

The overall collection efficiency increases for higher precipitation intensities, due to the increased numbers of larger equivalent diameter crystals with higher fall velocities. This results from changes in the exponential factor in the hydrometeor size distribution with precipitation intensity, as shown by Gunn and Marshall (1957). Their work was based on ground-level filter

595   paper measurements of equivalent hydrometeor diameters, representing the hydrometeor mass, instead of snowflake geometry. The hydrometeor size distribution of Gunn and Marshall has a lower offset and more rapid decay than that presented by Thériault et al. (2012), which is based on the measured snowflake diameter. Integrating the Gunn and Marshall drop size distribution, equivalent hydrometeor diameter, and fall velocity over the entire range of equivalent hydrometeor diameters gives a mutually consistent estimate for the precipitation intensity, supporting its use. Differences in collection efficiency with

600   solid precipitation intensity are not well understood, and are difficult to distinguish from gauge uncertainties due to

environmental conditions (e.g. wind, temperature). Regardless, these results demonstrate the variability in collection efficiency associated with the measurement of solid precipitation, even for hydrometeors of the same crystal habit.

The difference in collection efficiency for different precipitation characteristics illustrates the large variability that can be expected when the characteristics (type, habit, precipitation intensity) or fall velocity are not considered. This variability 605 presents a particular challenge for mixed precipitation conditions in which the precipitation type may not be well defined and can change rapidly over time. Both the wind speed and hydrometeor characteristics play important roles in determining collection efficiency. The proposed expression for the collection efficiency as a function of the wind speed and hydrometeor fall velocity (Eq. 18) provides a means of estimating the collection efficiency over different hydrometeor types and intensities, even if the precipitation type is not well defined.

4.4.3 Precipitation intensity dependence

610

Knowledge of the precipitation type, intensity, and wind speed can provide a means for adjusting gauge catchment totals. For rainfall, the precipitation intensity has been shown to be an important parameter for the estimation of overall collection efficiency (Nešpor and Sevruk, 1999;Jarraud, 2008). Overall collection efficiencies for rainfall are generally close to 1 based on the results of Sect. 3.4.3 and shown in Fig. 10. A gradual increase in overall collection efficiency with precipitation intensity 615 is observed for intensity values above 1 mm h^{-1}. Below this intensity, the overall collection efficiency decreases more rapidly, with the rate of decrease depending on the rainfall type and wind speed. This is in general agreement with the results of Nešpor and Sevruk as presented in Jarraud (2008), who showed a sharper increase in the conversion factor (inverse of overall collection efficiency) below 1 mm h^{-1}.

Overall collection efficiencies for snowfall also increase with precipitation intensity, as higher intensities correspond with 620 larger numbers of hydrometeors with higher fall velocities and increased collection efficiencies. Overall collection efficiencies for snowfall can be much lower than for rain, depending on the wind speed. Differences are apparent across different snowfall crystal habits (e.g. dendrites vs. dendrites and aggregates of plates), with the magnitude of differences increasing with wind speed. This illustrates the difficulty of adjusting snowfall measurements if the crystal habit is not known. The range of possible overall collection efficiency values is even larger under conditions when solid, liquid, or mixed precipitation can be present. 625 An additional challenge is presented by the measurement of low precipitation intensities for snowfall, where accumulations can be small relative to gauge uncertainties due to environmental factors (e.g. wind, temperature).

4.4.4 Hydrometeor fall velocity dependence

At a given wind speed, the relationship between the overall collection efficiency and hydrometeor fall velocity shown in Fig. 11 exhibits more uniform profiles for different hydrometeor types and size distributions than the relationship between overall 630 collection efficiency and precipitation intensity shown in Fig. 10. The hydrometeor type and size distribution influence the mass-weighted distribution of fall velocities, which, in turn, influence the ability of hydrometeors to be captured by the gauge at a given wind speed. The results in Fig. 11 follow the general nonlinear profile of the empirical expression (Eq. 18, Fig. 7),

with the hydrometeor fall velocity defining the overall collection efficiency magnitude for a given wind speed. Thunderstorm rain with hydrometeor fall velocities above 3.5 m s^{-1} exhibits the highest overall collection efficiencies, with values close to 1,

635 followed by orographic rain, and then the different snowfall types with lower fall velocities decreasing towards 0. Dendrites, which have the lowest fall velocities, exhibit the lowest overall collection efficiencies. Rimed dendrites have higher hydrometeor fall velocities relative to dendrites, and correspondingly higher overall collection efficiencies. Dendrites and aggregates of plates exhibit a large range of fall velocities that depends on the size distribution, giving rise to a large range in collection efficiencies.

640 The small differences in collection efficiency across different hydrometeor types with the same fall velocity are attributed to the nonlinearity in the relationship between collection efficiency and fall velocity over the mass-weighted distribution of hydrometeor fall velocities. Overall collection efficiency differences across precipitation types are much smaller when stratified by wind speed and hydrometeor fall velocity (Fig. 11) than when stratified by wind speed and precipitation intensity (Fig. 10) or by wind speed alone (Fig. 9). This results from the ability of the hydrometeor fall velocity to capture differences

645 in the overall collection efficiency across different hydrometeor types and precipitation intensities.

Measurements of fall velocity can be obtained using a number of methods (Sect. 4.2), and are increasingly available through the deployment of disdrometers in operational networks. These measurements provide an independent assessment of the hydrometeor fall velocity, and together with gauge height wind speed estimates, can enable the adjustment of gauge precipitation accumulation measurements using Eq. (18). Adjustments using this approach can be applied over a range of

650 hydrometeor types and even when the hydrometeor type may be unknown or uncertain.

5 Conclusions

Numerical modelling analysis is presented for an unshielded Geonor T-200B3 600 mm precipitation gauge. The gauge collection efficiency decreases nonlinearly with increasing wind speed and decreasing hydrometeor fall velocity. The model results illustrate that wind speed influences the updraft magnitude and local airflow around the gauge orifice, while fall velocity

655 affects the approach angle and degree of coupling between the hydrometeor trajectories and the local airflow. At a given wind speed, the collection efficiency varies from close to 0 for hydrometeor fall velocities below 1 m s^{-1} and approaching 1 for hydrometeor fall velocities above 2.5 m s^{-1}. Critically, collection efficiencies are similar for hydrometeors with different sizes, densities, and masses, but identical fall velocities.

An empirical expression derived from the modelling results captures well the nonlinear decrease in collection efficiency with

660 wind speed and hydrometeor fall velocity for several precipitation types, with a RMSE of 0.03. This expression provides comparable results to existing collection efficiency models for dry snow and wet snow for the unshielded Geonor T200-B3 gauge. Extending the application to orographic rain, thunderstorm rain, dendrites and aggregates of plates, rimed dendrites, and dendrites illustrates the large variability of overall collection efficiencies depending on the hydrometeor type and precipitation intensity. Adjustments based on the wind speed and hydrometeor fall velocity are shown to significantly reduce

665   this variability, and can be applied even where the precipitation type is unknown or uncertain, including mixed precipitation events. Hence, the empirical expression derived in this study can be applied to reduce the uncertainty in the overall collection efficiency, provided accurate estimates of the hydrometeor fall velocity are available.

670   *Author contribution.* J.H. was the lead author and was responsible for the CFD analysis, methodology, visualization, and manuscript preparation and editing. P.E.S. provided guidance for the analysis, interpretation of results, and writing – review and editing. P.I.J. provided guidance for the analysis, interpretation of results, visualization, and writing – review and editing. M.E.E. provided guidance for the interpretation of results, visualization, and writing – review and editing.

675   *Acknowledgements.* The authors would like to acknowledge the encouragement and support of Rodica Nitu for this field of study. Thanks to Christine Best, Pierrette Blanchard, and Sorin Pinzariu for supporting this work. Thank-you to the team members of the World Meteorological Organization Solid Precipitation Intercomparison Experiment (WMO-SPICE) who inspired this work.

680   *Data availability.* The flow simulation and collection efficiency results from this study shown in Figs. 3, 5, 8, 9, 10, and 11 will be made available in a suitable online repository.

Competing interests. The authors declare that they have no conflict of interest.

685   **References**

Atlas, D.: Optical extinction by rainfall, Journal of Meteorology, 10, 486-488, https://doi.org/10.1175/1520-0469(1953)010<0486:OEBR>2.0.CO;2, 1953.

Baghapour, B., and Sullivan, P. E.: A CFD study of the influence of turbulence on undercatch of precipitation gauges, Atmospheric Research, 197, 265-276, https://doi.org/10.1016/j.atmosres.2017.07.008, 2017.

690   Baghapour, B., Wei, C., and Sullivan, P. E.: Numerical simulation of wind-induced turbulence over precipitation gauges, Atmospheric Research, 189, 82-98, https://doi.org/10.1016/j.atmosres.2017.01.016, 2017.

Beard, K. V., and Pruppacher, H. R.: A determination of the terminal velocity and drag of small water drops by means of a wind tunnel, Journal of Atmospheric Sciences, 26, https://doi.org/10.1175/1520-0469(1969)026<1066:ADOTTV>2.0.CO;2, 1969.

Beard, K. V.: Terminal velocity and shape of cloud and precipitation drops aloft, J. Atmos. Sci., 33, 851-864, https://doi.org/10.1175/1520-0469(1976)033<0851:TVASOC>2.0.CO;2, 1976.

695   Biral micro rain radar: https://www.biral.com/product/micro-rain-radar/, access: June 25, 2019, 2019.

Blanchard, D. C.: Raindrop size distribution in Hawaiian rains, J. Meteor., 10, 457-473, https://doi.org/10.1175/1520-0469(1953)010<0457:RSDIHR>2.0.CO;2, 1953.

Bloemink, H. J. I., and Lanzinger, E.: Precipitation type from Thies disdrometers, Bucharest, Romania, 4-7, 2005.

700 Colli, M.: Assessing the accuracy of precipitation gauges: a CFD approach to model wind induced errors, PhD, Department of Civil, Chemical and Environmental Engineering, University of Genova, 2014.

Colli, M., Rasmussen, R., Thériault, J. M., L.G., L., Baker, B., and Kochendorfer, J.: An improved trajectory model to evaluate the collection performance of snow gauges, J. App. Met. & Clim., 54, 1826-1836, https://doi.org/10.1175/JAMC-D-15-0035.1, 2015.

Colli, M., Lanza, L. G., Rasmussen, R., and Thériault, J. M.: The collection efficiency of shielded and unshielded precipitation gauges. Part
705 I: CFD airflow modeling, J. Hydromet., 17, 231-243, https://doi.org/10.1175/JHM-D-15-0010.1, 2016a.

Colli, M., Lanza, L. G., Rasmussen, R., and Thériault, J. M.: The collection efficiency of shielded and unshielded precipitation gauges. Part II: Modeling particle trajectories., J. Hydromet., 17, 245-255, https://doi.org/10.1175/JHM-D-15-0011.1, 2016b.

Colli, M., Pollock, M., Stagnaro, M., Lanza, L. G., Dutton, M., and O'Connell, E.: A computational fluid-dynamics assessment of the improved performance of aerodynamic rain gauges, Water Resources Research, 54, 779-796, https://doi.org/10.1002/2017WR020549,
710 2018.

Constantinescu, G. S., Krajewski, W. F., Ozdemir, C. E., and Tokyay, T.: Simulation of airflow around rain gauges: comparison of LES and RANS models, Adv. Water Resour., 30, 43-58, https://doi.org/10.1016/j.advwatres.2006.02.011, 2007.

Goodison, B. E., Louie, P. Y. T., and Yang, D.: WMO solid precipitation measurement intercomparisonWMO/TD 872, 1998.

Gunn, K. L. S., and Marshall, J. S.: The distribution with size of aggregate snowflakes, Journal of Meteorology, 15, 452-461,
715 https://doi.org/10.1175/1520-0469(1958)015<0452:TDWSOA>2.0.CO;2, 1957.

Gunn, R., and Kinzer, G. D.: The terminal velocity of fall for water droplets in stagnant air., J. Meteor., 6, 243-248, https://doi.org/10.1175/1520-0469(1949)006<0243:TTVOFF>2.0.CO;2, 1949.

Haider, A., and Levenspiel, O.: Drag coefficient and terminal velocity of spherical and nonsperical particles, Powder technology, 58, 63-70, https://doi.org/10.1016/0032-5910(89)80008-7, 1989.

720 Henderson, C. B.: Drag coefficients of spheres in continuum and rarefied flows, American Institute of Aeronautics & Astronautics Journal, 14, 707-708, https://doi.org/10.2514/3.61409, 1976.

Imai, I., Fujiwara, M., Ichimura, I., and Toyama, Y.: Radar reflectivity of falling snow, Meteor. and Geophys. (Japan), 6, 130-139, https://doi.org/10.2467/mripapers1950.6.2_130, 1955.

Jarraud, M.: Guide to meteorological instruments and methods of observation, World Meteorological Organization, Geneva, Switzerland,
725 2008.

Kato, M., and Launder, B.: The modelling of turbulent flow around stationary and vibrating square cylinders, Ninth Symposium of Turbulent Shear Flows, Kyoto, Japan, 1993.

Khvorostyanov, V. I., and Curry, J. A.: Fall velocities of hydrometeors in the atmosphere: refinements to a continuous analytical power law, Journal of Atmospheric Sciences, 62, 4343-4357, https://doi.org/10.1175/JAS3622.1, 2005.

730 Kneifel, S., Von Lerber, A., Tiira, J., Moisseev, D., Kol-lias, P., and Leinonen, J.: Observed relations between snowfall microphysics and triple-frequency radar measurements, J. Geophys. Res.-Atmos., 120, 6034-6055, https://doi.org/10.1002/2015JD023156, 2015.

Kochendorfer, J., Rasmussen, R., Wolff, M., Baker, B., Hall, M. E., Meyers, T., Landolt, S., Jachcik, A., Isaksen, K., Braekkan, R., and Leeper, R.: The quantification and correction of wind-induced precipitation measurement errors, Hydrol. Earth Syst. Sci., 1793-1989, https://doi.org/10.5194/hess-21-1973-2017, 2017.

735 Kochendorfer, J., Nitu, R., Wolff, M., Mekis, E., Rasmussen, R., Baker, B., M.E., E., Reverdin, A., Wong, K., Smith, C. D., Yang, D., Roulet, Y.-A., Meyers, T., Buisan, S., Isaksen, K., Braekkan, R., Landolt, S., and Jachcik, A.: Testing and development of transfer functions for weighing precipitation gauges in WMO-SPICE, Hydol. Earth Syst. Sci., 22, 1437-1452, https://doi.org/10.5194/hess-22-1437-2018, 2018.

Langleben, M. P.: The terminal velocity of snowflakes, Quarterly Journal of the Royal Meteorological Society, 80, 174-181,
740 https://doi.org/10.1002/qj.49708034404, 1954.

Launder, B., and Spalding, D.: The numerical computation of turbulent flows, Computer methods in applied mechanics and engineering, 3, 269-289, https://doi.org/10.1016/B978-0-08-030937-8.50016-7, 1974.

Laws, J. O.: Measurements of the fall velocity of water drops and rain drops, Trans. Amer. Geophys. Union, 22, 709-721, https://doi.org/10.1029/TR022i003p00709, 1941.

745 Loffler-Mang, M., and Joss, J.: An optical distdrometer for measuring size and velocity of hydrometeors, JOAT, 130-139, https://doi.org/10.1175/1520-0426(2000)017<0130:AODFMS>2.0.CO;2, 2000.

Marshall, J. S., and Palmer, W. M.: The distribution of raindrops with size, Journal of Meteorology, 5, 165-166, https://doi.org/10.1175/1520-0469(1948)005<0165:TDORWS>2.0.CO;2, 1948.

Nešpor, V.: Investigation of wind-induced error of precipitation measurements using a three-dimensional numerical simulation, Department
750 of Geography, Swiss Federal Institute of Technology, Winterthurerstr. 190, 8057 Zurich, Switzerland, 117 pp., 1996.

Nešpor, V., and Sevruk, B.: Estimation of wind-induced error of rainfall gauge measurements using a numerical simulation, Journal of Atmospheric & Oceanic Technology, 16, 450-464, https://doi.org/10.1175/1520-0426(1999)016<0450:EOWIEO>2.0.CO;2, 1999.

Nitu, R., Roulet, Y.-A., Wolff, M., Earle, M., Reverdin, A., Smith, C., Kochendorfer, J., Morin, S., Rasmussen, R., Wong, K., Alastrué, J., Arnold, L., Baker, B., Buisán, S., Collado, J. L., Colli, M., Collins, B., Gaydos, A., Hannula, H.-R., Hoover, J., Joe, P., Kontu, A., Laine,
755 T., Lanza, L., Lanzinger, E., Lee, G., Lejeune, Y., Leppänen, L., Mekis, E., Panel, J.-M., Poikonen, A., Ryu, S., Sabatini, F., Theriault, J., Yang, D., Genthon, C., Heuvel, F. v. d., Hirasawa, N., Konishi, H., Nishimura, K., and Senese, A.: WMO Solid Precipitation Intercomparison Experiment (SPICE), World Meteorological Organization131, 2018.

Nitu, R. W., K.: CIMO Survey on National Summaries of Methods and Instruments for Solid Precipitation Measurement at Automatic Weather Stations, World Meteorological Organization, Geneva, SwitzerlandIOM Report-No. 102, 2010.

760 Ramana, M., Gupta, B. V., and Gupta, S. C.: Precipitation characteristics based on raindrop size measurements at Delhi and Khandala during southwest monsoon., J. Sci. Ind. Res., 18A, 352-371, 1959.

Rasmussen, R., Baker, B., Kochendorfer, J., Meyers, T., Landolt, S., Fischer, A. P., Black, J., Theriault, J. M., Kucera, P., Gochis, D., Smith, C., Nitu, R., Hall, M., Ikeda, K., and Gutmann, E.: How well are we measuring snow: the NOAA/FEE/NCAR winter precipitation test bed, BAMS, http://dx.doi.org/10.1175/BAMS-D-11-00052.1, 2012.

765 Rasmussen, R. M., Vivekanandan, J., and Cole, J.: The estimation of snowfall rate using visibility, Journal of Applied Meteorology, 38, 1542-1563, https://doi.org/10.1175/1520-0450(1999)038<1542:TEOSRU>2.0.CO;2, 1998.

Sevruk, B. H., J.-A.; Tettamanti, R.: The effect of orifice rim thickness on the wind speed above precipitation gauges, Atmospheric Environment, 28, 1939-1944, https://doi.org/10.1016/1352-2310(94)90334-4, 1994.

Sheppard, B. E., and Joe, P. I.: Automated precipitation detection and typing in winter: a two-year study, J. Atmos. Oceanic Technol., 17,
770 1493-1507, https://doi.org/10.1175/1520-0426(2000)017<1493:APDATI>2.0.CO;2, 2000.

Smith, C. D.: Correcting the wind bias in snowfall measurements made with a Geonor T-200B precipitation gauge and alter wind shield, 87th Annual AMS Meeting, San Antonio, TX, 2007.

SolidWorks: Enhanced turbulence modeling in SolidWorks flow simulation, USAMKTURBMODWPENG0313, 2013.

SolidWorks: SolidWorks Flow Simulation Technical Reference, 2019.

775 Spalding, D. B.: A single formula for the law of the wall, J. Appl. Mech., 28, 455-458, 1961.

Thériault, J. M., Rasmussen, R., Ikeda, K., and Landolt, S.: Dependence of Snow Gauge Collection Efficiency on Snowflake Characteristics, Journal of Applied Meteorology & Climatology, 51, https://doi.org/10.1175/JAMC-D-11-0116.1, 2012.

Thériault, J. M., Rasmussen, R., Petro, E., Trépanier, J.-Y., Colli, M., and Lanza, L. G.: Impact of wind direction, wind speed, and particle characteristics on the collection efficiency of the double fence intercomparison reference, Journal of Applied Meteorology and
780 Climatology, 54, 1918-1930, https://doi.org/10.1175/JAMC-D-15-0034.1, 2015.

Ulbrich, C. W.: Natural variations in the analytical form of the raindrop size distribution, Journal of Climate and Applied Meteorology, 22, 1764-1775, https://doi.org/10.1175/1520-0450(1983)022<1764:NVITAF>2.0.CO;2, 1983.

Wolff, M. A., Isaksen, K., Petersen-Øverleir, A., Ødemark, K., Reitan, T., and Brækkan, R.: Derivation of a new continuous adjustment function for correcting wind-induced loss of solid precipitation: results of a Norwegian field study, Hydrol. Earth Syst. Sci., 19, 951-
785 967, https://doi.org/10.5194/hess-19-951-2015, 2015.